Additive manufacturing of bioactive and biodegradable porous iron-akermanite composites for bone regeneration

Putra, N. E.; Borg, K. G.N.; Diaz-Payno, P. J.; Leeflang, M. A.; Klimopoulou, M.; Taheri, P.; Mol, J. M.C.; Fratila-Apachitei, L. E.; Zhou, J.; Zadpoor, A. A.

DOI
10.1016/j.actbio.2022.06.009

Publication date
2022

Document Version
Final published version

Published in
Acta Biomaterialia

Citation (APA)
Putra, N. E., Borg, K. G. N., Diaz-Payno, P. J., Leeflang, M. A., Klimopoulou, M., Taheri, P., Mol, J. M. C., Fratila-Apachitei, L. E., Zhou, J., Zadpoor, A. A., & More Authors (2022). Additive manufacturing of bioactive and biodegradable porous iron-akermanite composites for bone regeneration. *Acta Biomaterialia*, *148*, 355-373. https://doi.org/10.1016/j.actbio.2022.06.009

Acta Biomaterialia 148 (2022) 355–373

Contents lists available at ScienceDirect

Acta Biomaterialia

journal homepage: www.elsevier.com/locate/actbio

Full length article

Additive manufacturing of bioactive and biodegradable porous iron-akermanite composites for bone regeneration

N.E. Putra[a,*], K.G.N. Borg[a], P.J. Diaz-Payno[a,b], M.A. Leeflang[a], M. Klimopoulou[a], P. Taheri[c], J.M.C. Mol[c], L.E. Fratila-Apachitei[a], Z. Huan[d], J. Chang[d], J. Zhou[a], A.A. Zadpoor[a]

[a] Department of Biomechanical Engineering, Faculty of Mechanical, Maritime, and Materials Engineering, Delft University of Technology, Mekelweg 2, 2628 CD Delft, the Netherlands
[b] Department of Orthopedics and Sports Medicine, Erasmus MC University Medical Center, Rotterdam, 3015GD, the Netherlands
[c] Department of Materials Science and Engineering, Faculty of Mechanical, Maritime, and Materials Engineering, Delft University of Technology, Mekelweg 2, 2628 CD Delft, the Netherlands
[d] Shanghai Institute of Ceramics, Chinese Academy of Sciences, 1295 Dingxi Road, Shanghai 200050, China

ARTICLE INFO

Article history:
Received 31 March 2022
Revised 1 June 2022
Accepted 3 June 2022
Available online 9 June 2022

Keywords:
Extrusion-based 3D printing
Biodegradable
Iron
Akermanite
Composite
Scaffold
Bone substitution

ABSTRACT

Advanced additive manufacturing techniques have been recently used to tackle the two fundamental challenges of biodegradable Fe-based bone-substituting materials, namely low rate of biodegradation and insufficient bioactivity. While additively manufactured porous iron has been somewhat successful in addressing the first challenge, the limited bioactivity of these biomaterials hinder their progress towards clinical application. Herein, we used extrusion-based 3D printing for additive manufacturing of iron-matrix composites containing silicate-based bioceramic particles (akermanite), thereby addressing both of the abovementioned challenges. We developed inks that carried iron and 5, 10, 15, or 20 vol% of akermanite powder mixtures for the 3D printing process and optimized the debinding and sintering steps to produce geometrically-ordered iron-akermanite composites with an open porosity of 69–71%. The composite scaffolds preserved the designed geometry and the original α-Fe and akermanite phases. The *in vitro* biodegradation rates of the composites were improved as much as 2.6 times the biodegradation rate of geometrically identical pure iron. The yield strengths and elastic moduli of the scaffolds remained within the range of the mechanical properties of the cancellous bone, even after 28 days of biodegradation. The composite scaffolds (10–20 vol% akermanite) demonstrated improved MC3T3-E1 cell adhesion and higher levels of cell proliferation. The cellular secretion of collagen type-1 and the alkaline phosphatase activity on the composite scaffolds (10–20 vol% akermanite) were, respectively higher than and comparable to Ti6Al4V in osteogenic medium. Taken together, these results clearly show the potential of 3D printed porous iron-akermanite composites for further development as promising bone substitutes.

Statement of significance

Porous iron matrix composites containing akermanite particles were produced by means of multi-material additive manufacturing to address the two fundamental challenges associated with biodegradable iron-based biomaterials, namely very low rate of biodegradation and insufficient bioactivity. Our porous iron-akermanite composites exhibited enhanced biodegradability and superior bioactivity compared to porous monolithic iron scaffolds. The murine bone cells proliferated on the composite scaffolds, and secreted the collagen type-1 matrix that stimulated bony-like mineralization. The results show the exceptional potential of the developed porous iron-based composite scaffolds for application as bone substitutes.

1. Introduction

Biodegradable iron-based biomaterials have been developed for several years to assist with the regeneration of critical size bone

---

[*] Corresponding author.
E-mail address: n.e.putra@tudelft.nl (N.E. Putra).

https://doi.org/10.1016/j.actbio.2022.06.009
1742-7061/

defects [1–4]. To aid in the regeneration of bone tissue, the biomaterials should (i) fit the anatomical site of the bone defect [5–7], (ii) have mechanical properties in the range of those of bone tissue to preclude the stress shielding effect [8–10], (iii) possess a high degree of interconnected porosity to facilitate angiogenesis, bone ingrowth, as well as the transport of nutrients [11–13], and (iv) biodegrade *in vivo* while providing the required level of mechanical support during the entire process of bone tissue regeneration [14–16]. To date, the low rate of *in vivo* biodegradation and the inadequate level of osteogenic properties have been the main hinderances preventing Fe-based bone substitutes from widespread clinical application [17].

From the mechanical viewpoint, the higher strength of bulk Fe as compared to other biodegradable metals (*e.g.*, Mg- or Zn-based biomaterials [18–20]) enables the design of bone-mimicking porous implants. The porosity of Fe scaffolds eliminates the stress-shielding effect, provides more surface area for biodegradation, and allows for bony ingrowth [21–23]. Numerous techniques have been used to enhance the biodegradation rate of Fe *in vitro*. For example, Fe has been alloyed with Ag [24,25], Mn [26–30], Mn-Ag [31–33] or Pd [34,35] to multiply microstructural phases with different nobility, hence triggering enhanced local corrosion through micro-galvanic interactions between the different phases. The recent advances in additive manufacturing techniques have enabled the fabrication of porous iron with exact geometrical designs to increase their biodegradation rate while maintaining their mechanical integrity over time [22,36,37]. While these two strategies (*i.e.*, alloying and making Fe structurally porous) address one of the above-mentioned challenges regarding the use of iron as a bone substituting biomaterial, they are incapable of providing iron with favorable bioactive properties that are required to stimulate bone regeneration. In fact, accelerated biodegradation of Fe can even negatively influence its biocompatibility because too much Fe^{2+} release can inhibit the *in vitro* metabolic activity of preosteoblasts [36,37]. Moreover, the addition of other alloying elements is unlikely to make the materials more biocompatible [38].

Here, we propose additively manufactured porous iron composites incorporating bioactive-degradable bioceramic particles to address both challenges simultaneously. For such composites, the relatively fast degradation of the bioceramic phase in Fe-matrix composites is expected at the beginning of the biodegradation period, increasing the initial biodegradation rate of the composite materials. Simultaneously, the dissolution of the bioceramic phase is expected to induce surface mineralization on the composite material, stimulating the adhesion, proliferation, and differentiation of osteoprogenitor cells [39]. With time, the dissolved bioceramic phase exposes additional surfaces inside the iron matrix for further biodegradation. To date, the Fe-based biocomposites have been developed with the reinforcement of hydroxyapatite (HA) [40–42], tricalcium phosphate (TCP) [43–45], calcium silicate ($CaSiO_3$) [46,47], magnesium silicide (Mg_2Si) [48–50], or bredigite ($Ca_7Mg(SiO_4)_4$) [51,52] using various fabrication methods. In general, the performance of several Fe-based biocomposites has been well acknowledged in improving both biodegradation and bioactivity of iron. Nevertheless, further research is still required to determine the appropriate choice of the bioceramic material and the optimum composition to provide the most effective biofunctionality for Fe-based biomaterials. Extrusion-based 3D printing has only been utilized for the fabrication of Fe-$CaSiO_3$ composite scaffolds [47].

In this study, we used akermanite ($Ca_2Mg(Si_2O_7)$) as the second structural component in the porous iron matrix to form composites that have not yet appeared in the literature. Recent developments in bioceramics for bone tissue engineering have shown Mg- and/or Si-based bioceramics to be promising alternatives to well-known Ca- and P-based bioceramics (*e.g.*, HA and TCP) [53,54]. For example, Mg has been found to stimulate the proliferation and osteogenic differentiation of osteoblasts [55]. In addition, Mg scaffolds have been shown to restore bone tissue *in vivo* successfully [56]. Likewise, Si can promote the synthesis of collagen type-1 and the calcification of the bony tissue [57,58]. Akermanite contains both Mg- and Si and *in vivo* studies have demonstrated that it can offer better osteogenic and angiogenic capabilities than TCP [59–61]. In addition, akermanite has been shown to significantly reduce the inflammatory responses of macrophages *in vivo* [62], allowing for better osseointegration.

Extrusion-based 3D printing of scaffolds for bone regeneration has been recently utilized for its merits in multi-material fabrication through alloying or compositing porous multi-functional Fe-based materials [30,47]. In this study, we used extrusion-based 3D printing technique for fabricating porous Fe-matrix composites with 5, 10, 15, and 20 vol% akermanite. We also comprehensively characterized the porous composites *in vitro* biodegradation behavior, the electrochemical response, the mechanical properties varying along with *in vitro* biodegradation, and the *in vitro* biological response of preosteoblasts to these new biomaterials.

2. Materials and methods

2.1. Iron powder and synthesis of akermanite powder

Iron powder (purity = 99.88 wt%; spherical morphology; particle size < 63 μm, Fig. 1a) was supplied by Material Technology Innovations Co. Ltd., China. Akermanite powder ($Ca_2MgSi_2O_7$; Mg wt% = 8.92; an irregular morphology; particle size < 45 μm, Fig. 1b) was synthesized by using the sol–gel process with the use of tetraethyl orthosilicate [$(C_2H_5O)_4Si$, TEOS], magnesium nitrate hexahydrate [$Mg(NO_3)_2 \cdot 6H_2O$], and calcium nitrate tetrahydrate [$Ca(NO_3)_2 \cdot 4H_2O$] as the raw materials [63], followed by a calcination step at 1300 °C for 3 h.

2.2. Iron-akermanite ink preparation and characterization

The iron and akermanite powder mixtures (with 5, 10, 15, and 20 vol% of akermanite, hereafter designated as Fe-5Ak, Fe-10Ak, Fe-15Ak, and Fe-20Ak, respectively) were prepared using a roller mixer (CAT Zipperer GmbH, Germany) at 80 rpm for 2 h. Then, the powder mixtures were blended with a water-based binder (made of a 5 wt% aqueous solution of hydroxypropyl methylcellulose with M_w ~86 kDa, from Sigma Aldrich, Germany [37]) to create iron-akermanite inks with a powder volume ratio of 47.45%. The rheological characteristics of the inks were observed using an MCR302 rheometer (Anton Paar GmbH, Germany) and the results are presented in the supplementary material. In addition, to understand the dissolution characteristics of akermanite in the ink during 3D printing, the akermanite powder was mixed with demineralized water (with mass values equal to those in the Fe-5Ak and Fe-20Ak inks) for 2 h. Then, the supernatant was filtered through a 0.22 μm filter (Merck Millipore, Germany). The dissolved ions in the supernatant were quantified using an inductively coupled plasma optical emission spectroscope (ICP-OES, iCAP 6500 Duo, Thermo Scientific, USA).

2.3. Extrusion-based 3D printing, debinding and sintering

Porous iron-akermanite scaffolds (with ϕ = 10 mm and h = 10.5 mm) were built through the extrusion of iron-akermanite inks using a 3D BioScaffolder 3.2 printer (GeSiM Bio-instruments and Microfluidics, Germany). A lay-down pattern design of 0°/90° switching every other layer was used. The design had a strut size of 410 μm and a strut spacing of 400 μm. The extrusion-based 3D printing was performed at a printing speed of 5 mm/s under

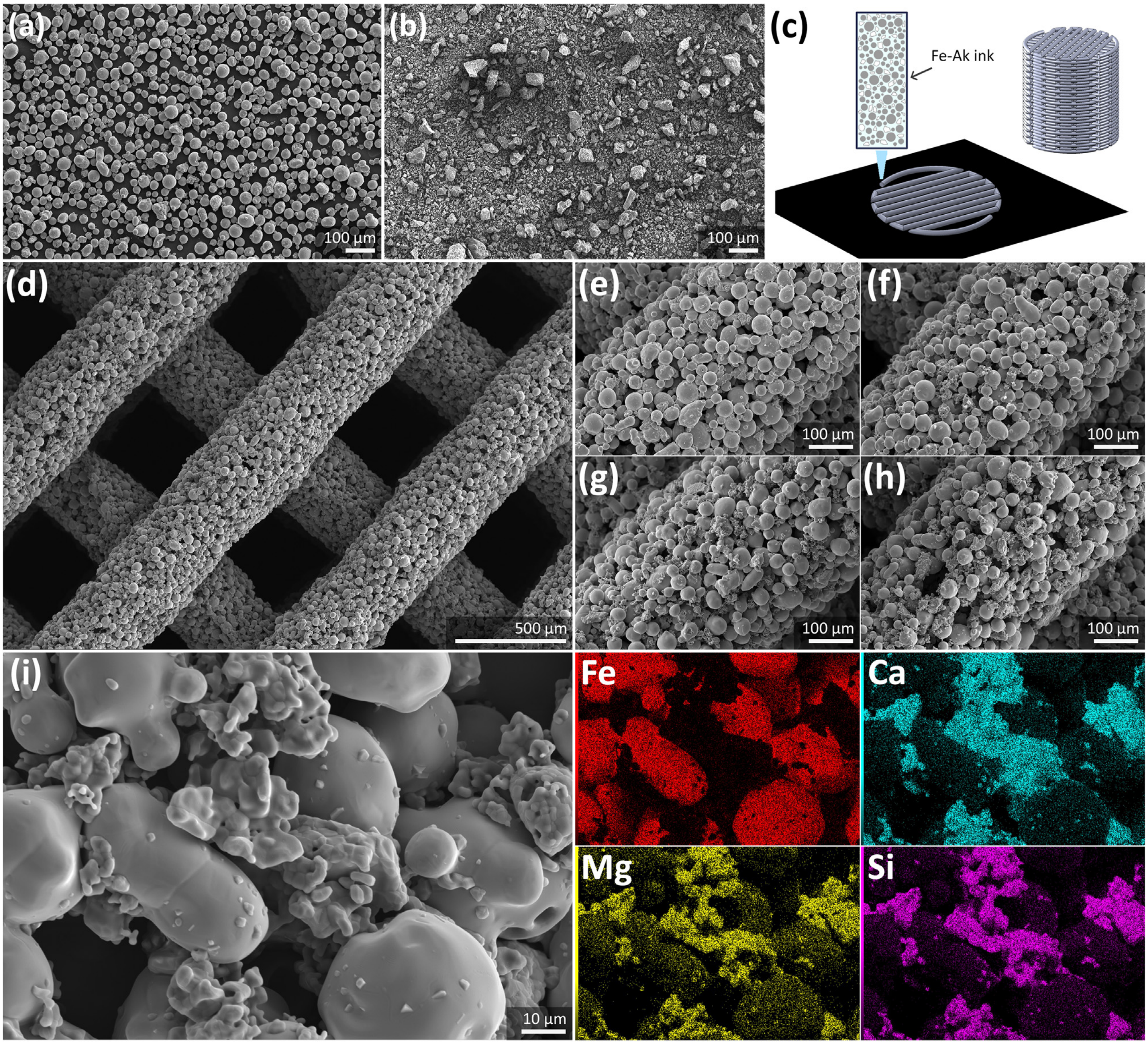

Fig. 1. The morphologies of the starting powder materials: (a) iron and (b) akermanite. (c) The extrusion-based 3D printing and the design of porous iron-akermanite scaffolds with a 0° and 90° laydown pattern. (d) The morphology of the porous iron-akermanite composite scaffolds and the strut morphologies of the (e) Fe-5Ak, (f) Fe-10Ak, (g) Fe-15Ak, and (h) Fe-20Ak composites at a higher magnification. (i) EDS elemental mapping on the periphery of the porous iron-akermanite struts.

the printing pressures of 175 kPa, 205 kPa, 235 kPa, and 250 kPa, respectively, for the Fe-5Ak, Fe-10Ak, Fe-15Ak, and Fe-20Ak inks. The green-body iron-akermanite scaffolds had a relative porosity of 50% and a surface area of 40.4 cm^2 (Fig. 1c). After 3D printing, the green-body scaffolds were placed inside a tube furnace (STF16/180, Carbolite Gero Ltd., UK) under highly pure argon flow (purity = 99.9999%; inlet gas pressure = 1 bar). A two-step heating cycle was applied including debinding at 350 °C for 1 h and sintering at 1200 °C for 6 h, followed by cooling. The as-sintered iron-akermanite composites were ultrasonically cleaned in isopropyl alcohol for 15 min and were stored in an argon-filled chamber for further investigations.

2.3. Characterization of porosity, microstructure and phase composition

The dimensional changes imparted during the sintering process were determined by measuring the diameter and height of the iron-akermanite composite scaffolds before and after sintering. The morphology of the composite scaffolds was observed using a scanning electron microscope (SEM, JEOL JSM-IT100, Japan). Moreover, the strut size and strut spacing were measured. The chemical composition of the struts was mapped using X-ray energy dispersive spectroscopy (EDS) (JEOL JSM-IT100, Japan). The phases present in the iron-akermanite composites were identified using an X-ray diffractometer (XRD, D8 Advance, Bruker, USA) in the Bragg-Brentano geometry, equipped with a graphite monochromator and a Lynxeye position-sensitive detector. XRD analysis was performed using Cu Kα radiation, at 45 kV and 40 mA, using a step size of 0.030° and a counting time of 2 s per step. The obtained XRD patterns were analyzed with the Diffrac Suite.EVA v5.2 software. On the cross-section of the composite scaffolds, the diffusion of iron into akermanite across the interfaces was inspected through EDS line analysis (JEOL JSM-IT100, Japan).

The porosities of the composite scaffolds were determined. Dry weighing was used to measure the absolute porosity (Eq. (1)) while oil impregnation was applied for the measurement of the interconnected porosity (Eq. (2)), based on the ASTM standard B963–13

[64]:

$$\varphi_a = \left(1 - \frac{m/\rho_{Fe-Ak}}{V_{bulk}}\right) \times 100\% \tag{1}$$

where φ_a is the absolute porosity [%], m is the mass [g] of the as-sintered composite scaffold, V_{bulk} is the bulk volume [cm^3], and $\rho_{Fe\text{-}Ak}$ is the theoretical density of the iron-akermanite composite (*i.e.*, 7.62 g/cm^3 for Fe-5Ak, 7.38 g/cm^3 for Fe-10Ak, 7.15 g/cm^3 for Fe-15Ak, and 6.84 g/cm^3 for Fe-20Ak).

$$\varphi_i = \left(\frac{\rho_{ethanol}}{\rho_{oil}} \times \frac{m_o - m_a}{m_o - m_{eo}}\right) \times 100\% \tag{2}$$

where φ_i is the interconnected porosity [%], $\rho_{ethanol}$ is the density of ethanol (*i.e.*, 0.789 g/cm^3), ρ_{oil} is the density of oil (*i.e.*, 0.919 g/cm^3), m_o and m_{eo} are, respectively, the masses of the oil-impregnated composite scaffolds weighed in air and in ethanol [g], and m_a is the mass of the composite scaffold weighed in air [g].

2.4. Biodegradation experiments

2.4.1. Immersion tests

The iron-akermanite composite scaffolds were immersed in a revised simulated body fluid (r-SBF) [65] with 6.7 mL of r-SBF per 1 cm^2 scaffold surface area [66] for 1, 4, 7, 14, and 28 d. The immersion tests were performed under static condition at 37 ± 0.5 °C with an initial pH of 7.40, a relative humidity (RH) of 95%, and an atmosphere containing 5% CO_2. Monolithic iron scaffolds [37] were also tested as the control group for the measurement of biodegradation rate. Prior to the immersion tests, the specimens ($n = 3$, for each time point) were sterilized and the r-SBF medium was filtered using a 0.22 µm pore size filter (Merck Millipore, Germany). The pH values of the r-SBF medium were monitored using a pH electrode (InLab Expert Pro-ISM, METTLER TOLEDO, Switzerland) during the *in vitro* immersion tests at selected time points.

2.4.2. Characterization of the biodegradation products

The concentrations of soluble Fe^{2+}, Ca^{2+}, Mg^{2+}, Si^{+}, and PO_4^{3-} ions in the r-SBF were measured at various time points using ICP-OES (iCAP 6500 Duo, Thermo Scientific, USA). Following immersion until the preselected time points, the specimens were retrieved and the morphologies and chemical compositions of the biodegradation products on the periphery and at the center of the scaffolds were examined using SEM and EDS (JEOL JSM-IT100, Japan). The phases present in the biodegradation products after immersion for 4 d and 28 d were identified using XRD (D8 Advance, Bruker, USA). The biodegradation rates of the iron-akermanite composite scaffolds at different time points were determined using mass loss measurements. Prior to the mass measurement, the as-biodegraded scaffolds were immersed in a solution containing hydrochloric acid and hexamethylene tetramine to remove the precipitated biodegradation products. The procedure was based on the ASTM standard G1–03 [67] and is described in detail in our previous publication [37]. After that, the remaining composite material was weighed and the average biodegradation rate was calculated, following the ASTM standard G31–72 [68]:

$$CR_{immersion}\,[mm/year] = 8.76 \times 10^4 \times \frac{m}{A \times t \times \rho} \tag{3}$$

where ρ is the theoretical density of the iron-akermanite composite (g/cm^3), t is the immersion period [h], A is the surface area of the porous iron-akermanite composite specimen [cm^2] calculated based on the initial scaffold design value, and m is the mass loss value [g].

2.4.3. Electrochemical measurements

The electrochemical response of the iron-akermanite composite scaffolds during biodegradation in the r-SBF medium at 37 ± 0.5 °C and with an initial pH of 7.40 was recorded using a Bio-Logic SP-200 potentiostat (Bio-Logic Science Instruments, France), following the parameters described elsewhere [30,37]. A three-electrode setup included an Ag/AgCl electrode (reference electrode), a graphite bar (counter electrode), and the composite specimen partially embedded in an acrylic resin (working electrode). The exposed surface area of the composite specimen was calculated based on the initial design value of the scaffold. Prior to linear polarization resistance (LPR) and electrochemical impedance spectroscopy (EIS) measurements, the electrode system was stabilized to a steady open circuit potential (OCP) for 1 h. Subsequently, the LPR and EIS measurements were performed for up to 28 d of immersion. The LPR values were measured at a scanning rate of 0.167 mV/s from −25 to +25 mV *vs.* OCP. The EIS measurements were conducted at frequencies ranging from 100 kHz to 10 mHz using a 10 mV sine amplitude *vs.* OCP.

2.5. Mechanical tests

Compression tests were performed using a universal material testing machine (Zwick Z100, Germany, with a 100 kN load cell) to evaluate the mechanical properties of the as-sintered and as-biodegraded iron-akermanite composite scaffolds ($n = 3$). The compression tests were carried out at a crosshead speed of 3 mm/min, following the ISO standard 13,314:2011 [69]. From the stress-strain curve, the quasi elastic gradient (referred as Young's modulus) and the compressive 0.2% offset stress (referred as yield strength) were determined. The Young's modulus value was obtained from the slope of the initial linear region of the stress-strain curve. The yield strength value was obtained from the stress value at the intersection of the stress-strain curve with a 0.2% offset line, parallel to the initial linear region of the curve.

2.6. Cytocompatibility evaluation

2.6.1. Preculture of preosteoblasts and cell culture medium

Murine MC3T3-E1 preosteoblasts (Sigma Aldrich, Germany) were precultured for 7 d in a cell culture incubator (temperature = 37 ± 0.5 °C, RH = 95%, and 5% CO_2). The cell culture medium contained the α-minimum essential medium (α-MEM, Thermo Fisher Scientific, USA) without ascorbic acid and was supplemented with 10% fetal bovine serum (FBS, Thermo Fisher Scientific, USA) and 1% penicillin/streptomycin (p/s, Thermo Fisher Scientific, USA). The same cell culture medium was used for all other cell culture assays, unless otherwise stated.

2.6.2. Preparation of iron-akermanite extracts and prestoblue assay

Extracts were obtained after 72 h of incubation of the sterile composite scaffolds ($\phi = 9.7$ mm and $h = 10.3$ mm; $n = 3$) in the cell culture medium with 1 mL medium for every 5 cm^2 of the specimen's surface area. The exposed surface area of the composite specimen was calculated based on the initial design value of the specimens. The extracts were filtered using a 0.22 µm pore size filter (Merck Millipore, Germany) and were diluted to 75%, 50%, and 25% of their original concentrations.

The preosteoblasts (1×10^4 cells) were cultured in a 48-well plate containing 200 µL iron-akermanite extracts for 1, 3, and 7 d ($n = 3$ for every extract concentration). The same preosteoblasts were cultured in the cell culture medium as the negative control. PrestoBlue assay (Thermo Fisher Scientific, USA) was utilized to evaluate the metabolic activity of the cells, following the procedure described in our previous publication [37]. At the selected cell culture time points, the PrestoBlue reagent was added to the wells and the metabolic activities of the cells were measured as the absorbance values at a wavelength of 530–590 nm using a microplate reader (Victor X3, PerkinElmer, The Netherlands).

$$\text{Metabolic activity [\%]} = \frac{\text{Absorbance (specimen)}}{\text{Absorbance (negative control)}} \times 100 \quad (4)$$

2.6.3. Trypan blue assay and live-dead staining

The preosteoblasts (5 × 10^4 cells per specimen) were seeded and cultured on the iron-akermanite composite specimens (ϕ = 9.7 mm and h = 1.3 mm) in 6-well plates with 8 mL of cell culture medium for 1, 4, 7, 14, and 28 d (n = 3 for every time point). Porous Ti6Al4V scaffolds were used as the reference material (positive control). The Trypan blue assay (Bio-Rad, USA), followed by cell counting steps using an automated cell counter (TC20, Bio-Rad, USA), was used to calculate the number of the preosteoblasts present at the selected cell culture time points. In addition, the distribution and the viability of preosteoblasts was evaluated using calcein (green = live) and ethidium homodimer-1 (red = dead) staining (Thermo Fisher Scientific, USA) after 7, 14, and 28 d of cell culture.

2.6.4. Morphology of preosteoblasts on the composite scaffolds

The morphology of the preosteoblasts after 7, 14, and 28 d of cell culture on the composite scaffolds (*i.e.*, Fe-10Ak, Fe-15Ak, and Fe-20Ak) was observed using SEM (JEOL JSM-IT100, Japan). Additionally, the strut morphology and associated biodegradation products formed on the composite scaffolds (immersed in the cell culture medium for 14 and 28 d without cells) were examined using SEM and EDS.

2.6.5. Collagen type-1 staining

After cell culture for 7, 14, and 28 d, the composite scaffolds (*i.e.*, Fe-10Ak, Fe-15Ak, and Fe-20Ak) were washed with phosphate buffer saline (PBS) and were fixed with 4% formaldehyde (Sigma Aldrich, Germany) for 15 min. Then, the specimens were washed with PBS and permeabilized using 0.5% Triton/PBS (Sigma Aldrich, Germany). Consecutively, the scaffolds were incubated with anti-collagen type-1 primary antibody (1:100 per specimen, Thermo Fisher Scientific, USA) in 1% bovine serum albumin (BSA)/PBS, followed by washing with 0.5% Tween/PBS (Sigma Aldrich, Germany). The second incubation step was performed using Alexa Fluor 488 conjugated secondary antibody (1:200, Thermo Fischer Scientific, USA) in 1% BSA/PBS, followed by washing with 0.5% Tween/PBS (Sigma Aldrich, Germany). Subsequently, the specimens were washed with PBS. Thereafter, the specimens were imaged using a fluorescence microscope (ZOE cell imager, Bio-Rad, USA).

2.6.6. Alkaline phosphatase (ALP) assay

The ALP activities of the preosteoblasts were determined after 14 and 28 d of culture on the composite scaffolds (*i.e.*, Fe-10Ak, Fe-15Ak, and Fe-20Ak) using a fluorometric ALP assay kit (ab83371, Abcam, Thermo Fisher Scientific, USA). Porous monolithic iron and Ti-6Al-4 V specimens were included as the negative and positive control groups, respectively. The positive control groups were cultured in the cell culture medium with additional osteogenic reagents (*i.e.*, ascorbic acid 1:1000 and β-glycerophosphate 1:500). The ALP measurements were conducted, following the steps described in the manufacturer's protocol. The ALP activities were reported in terms of fold-change against the negative control.

2.7. Statistical analysis

The statistical analysis of the cell counting results was performed with two-way ANOVA, followed by a Tukey multiple comparison *post hoc* test ($^{****} = p < 0.0001$, $^{***} = p < 0.001$, $^{**} = p < 0.01$, and $^{*} = p < 0.05$, *n.s.* = not significant).

Table 1
Structural characteristics of the extrusion-based 3D printed porous iron-akermanite scaffolds.

Sample group	Strut width (µm)	Strut spacing (µm)
Fe-5Ak	407 ± 8	402 ± 7
Fe-10Ak	408 ± 7	403 ± 9
Fe-15Ak	407 ± 7	403 ± 8
Fe-20Ak	408 ± 6	401 ± 6

3. Results

3.1. Characteristics of the porous iron-akermanite composite scaffolds

The porous iron-akermanite scaffolds fabricated through extrusion-based 3D printing (**Figure S1**) closely followed the geometrical 0° and 90° lay-down pattern design even after the debinding and sintering cycle steps (Fig. 1d, Table 1). Successful extrusion-based 3D printing of iron-akermanite-containing inks strongly relies on adequate powder loading in the ink and its shear-thinning behavior (**Figure S2**). Due to sintering, the diameter and height of the composite scaffolds reduced by 2.7–3.4% and 1.9–2.1%, respectively. The struts of the composite scaffolds, nevertheless, continued to feature a random micro-porous structure (Fig. 1d). The volume fraction of akermanite clearly increased, given the more irregularly shaped powder particles dispersed across the struts (Fig. 1e-h). In addition to the sintered iron and akermanite powder particles, smaller akermanite particles adhering to the surfaces of iron particles were observed (Fig. 1i). EDS mapping analysis detected Ca, Mg, and Si covering the surface of iron powder particles (Fig. 1i).

The iron-akermanite composite scaffolds had interconnected porosities of 70 ± 1%, 69 ± 3%, 69 ± 1%, and 71 ± 1% for the Fe-5Ak, Fe-10Ak, Fe-15Ak, and Fe-20Ak groups, respectively. The increasing akermanite volume in the iron matrix did not significantly influence the porosity of the specimens (Fig. 2a). The XRD patterns displayed the α-Fe phase and $Ca_2Mg(Si_2O_7)$ phase in the porous iron-akermanite scaffolds with no additional crystalline compounds (Fig. 2c). The intensity of the akermanite phase was relatively higher in the scaffold with a higher akermanite volume fraction. On the cross-section of the struts, the iron and akermanite powder particles were observed to have undergone thorough co-sintering (Fig. 2b). It was clear that the base material (gray color) belonged to iron and the dispersed particles (dark gray color) were akermanite. At a higher magnification, the interface between iron and akermanite revealed on the cross-section of the Fe-20Ak specimens (Fig. 2d) did not show any additional compounds formed and was free from any noticeable defects. Elemental diffusion from the iron phase to the akermanite phase occurred up to a depth of approximately 1.7 µm (Fig. 2d).

3.2. *In vitro* biodegradation behavior

After 1 d of *in vitro* immersion, the iron-akermanite composite scaffolds were covered by a layer of dark brown biodegradation products. The biodegradation products grew thicker into a yellow-brownish color during further immersion for up to 28 d (Fig. 3a). The global pH value of the r-SBF medium maintained between 7.62 and 7.65 throughout the biodegradation period. The mass of the composite scaffolds decreased due to biodegradation. The mass loss percentage increased during the first 4 d of immersion followed by a reduction to 7 d of immersion and the increases corresponding to 14 d and 28 d of immersion (Fig. 3b). A larger mass loss was observed in the composite scaffold with a higher akermanite volume fraction. At day 14 of biodegradation, the degradation rates of the porous iron-akermanite scaf-

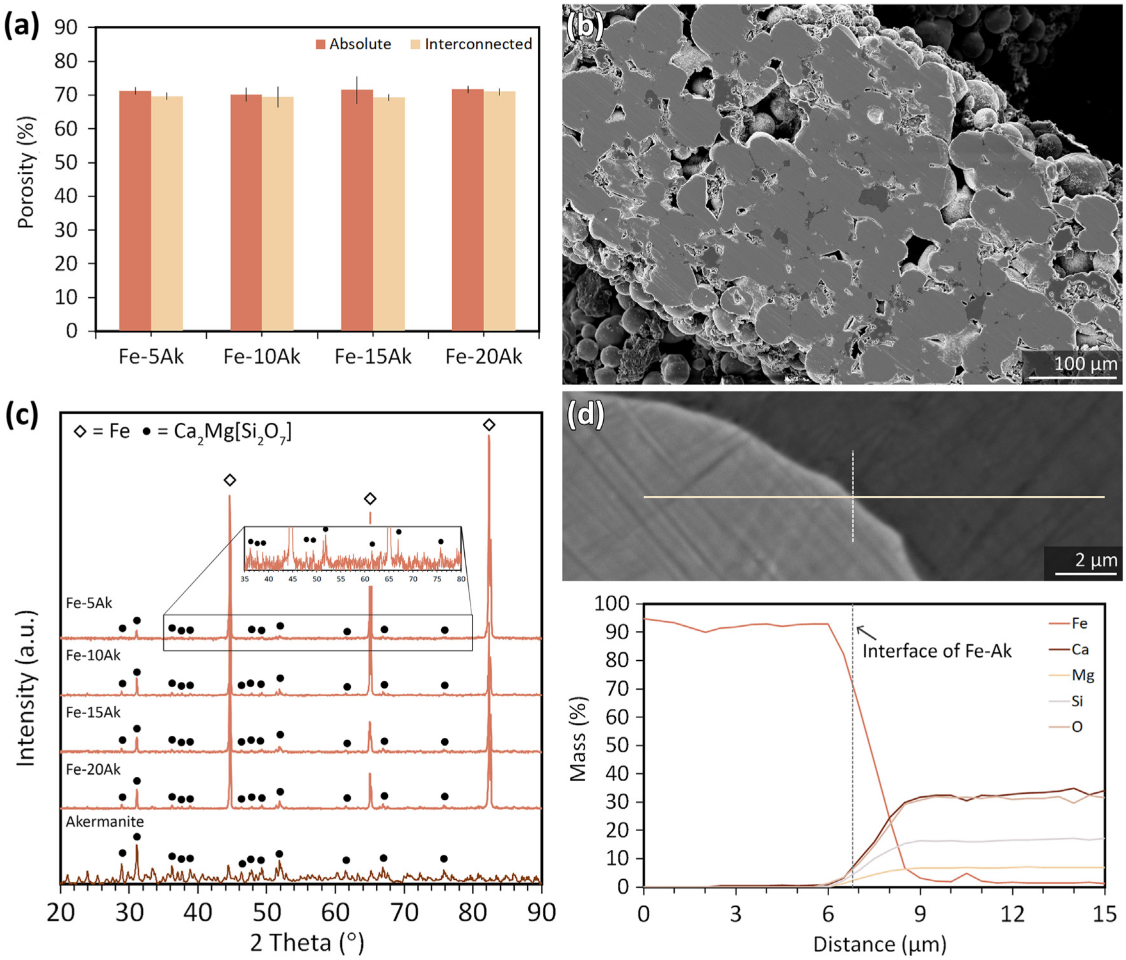

Fig. 2. (a) The porosities of the iron-akermanite composite scaffolds, (b) the cross-section of the struts, (c) the phase composition of akermanite powder and the composite scaffolds and (d) the EDS line analysis across the interfaces of iron and akermanite.

folds were 0.14 ± 0.01 mm/y, 0.16 ± 0.02 mm/y, 0.20 ± 0.01, and 0.24 ± 0.02 mm/y for Fe-5Ak, Fe-10Ak, Fe-15Ak, and Fe-20Ak, respectively. At the end of the immersion tests (*i.e.*, day 28), the *in vitro* biodegradation rates of the porous iron-akermanite scaffolds were 0.08 ± 0.01 mm/y, 0.09 ± 0.01 mm/y, 0.11 ± 0.02 mm/y, and 0.13 ± 0.01 mm/y for Fe-5Ak, Fe-10Ak, Fe-15Ak, and Fe-20Ak, respectively (Fig. 3c). For comparison, the porous monolithic iron showed the degradation rates of 0.09 ± 0.02 mm/y at day 14 and 0.05 ± 0.02 mm/y at day 28 [37].

During biodegradation, Fe^{2+}, Ca^{2+}, Mg^{2+}, and Si^{+} were steadily released to the r-SBF medium (Fig. 4). The Fe^{2+} concentrations reached their peaks at day 14 (*i.e.*, 0.17 to 0.30 mg/L) and the ion release decreased towards the end of the immersion period (Fig. 4a). In the case of the Fe-15Ak and Fe-20Ak specimens, the Ca^{2+}concentrations detected in the solution were higher at all time points as compared to the initial Ca^{2+}concentration in the r-SBF medium (*i.e.*, 121.1 to 132.4 mg/L at day 28, Fig. 4b). On the other hand, the Ca^{2+} concentrations in the solution corresponding to the Fe-5Ak and Fe-10Ak specimens remained largely unchanged in the first 7 d of immersion, but slightly reduced towards the end of immersion (*i.e.*, 85.8 to 96.6 mg/L at day 28, Fig. 4b). At the same period of immersion, the Mg^{2+} and Si^{+} concentrations steadily increased (*i.e.*, 52.0 to 77.4 mg/L and 21.7 to 26.9 mg/L, respectively, Fig. 4c-d). As for the PO_4^{3-} ions in the r-SBF medium, the concentrations continually declined throughout the 28 d of immersion (Fig. 4e).

3.3. Characteristics of the biodegradation products on scaffold surfaces

The main phase in the peripheral degradation products of the porous iron-akermanite composites after 4 d and 28 d of immersion was lepidocrocite (γ-FeOOH) (Fig. 3d-e). The calcite ($CaCO_3$) phase was detected on the Fe-15Ak and Fe-20Ak scaffolds after 4 d of immersion (Fig. 3d) and its intensity increased towards 28 d of immersion (Fig. 3e). By contrast, the $CaCO_3$ phase was observed on the Fe-5Ak and Fe-10Ak scaffolds only after 28 d of immersion (Fig. 3e). From the SEM micrographs, the struts of the composite scaffolds were fully enveloped by the degradation products as early as day 4 of the immersion tests (Fig. 5a-c). The biodegradation products transformed into a denser structure throughout the immersion period (Fig. 5, **S4–6**).

The morphology of the peripheral biodegradation products was discernible in two major forms (Fig. 5): a fine, particulate porous structure and coral-like precipitates decorating the surfaces. The coral-like degradation products were rich in Ca, while the porous particulate surfaces contained more Fe (Table 2). These elements corresponded to the phase compositions identified by XRD. On the Fe-20Ak composite scaffolds, the coral-like precipitates expanded over the biodegradation time, covering the particulate corrosion products (Fig. 5). Similar observations were noted for the Fe-15Ak (**Figure S4, Table S1**), Fe-10Ak (**Figure S5, Table S2**) and Fe-5Ak (**Figure S6, Table S3**) composites.

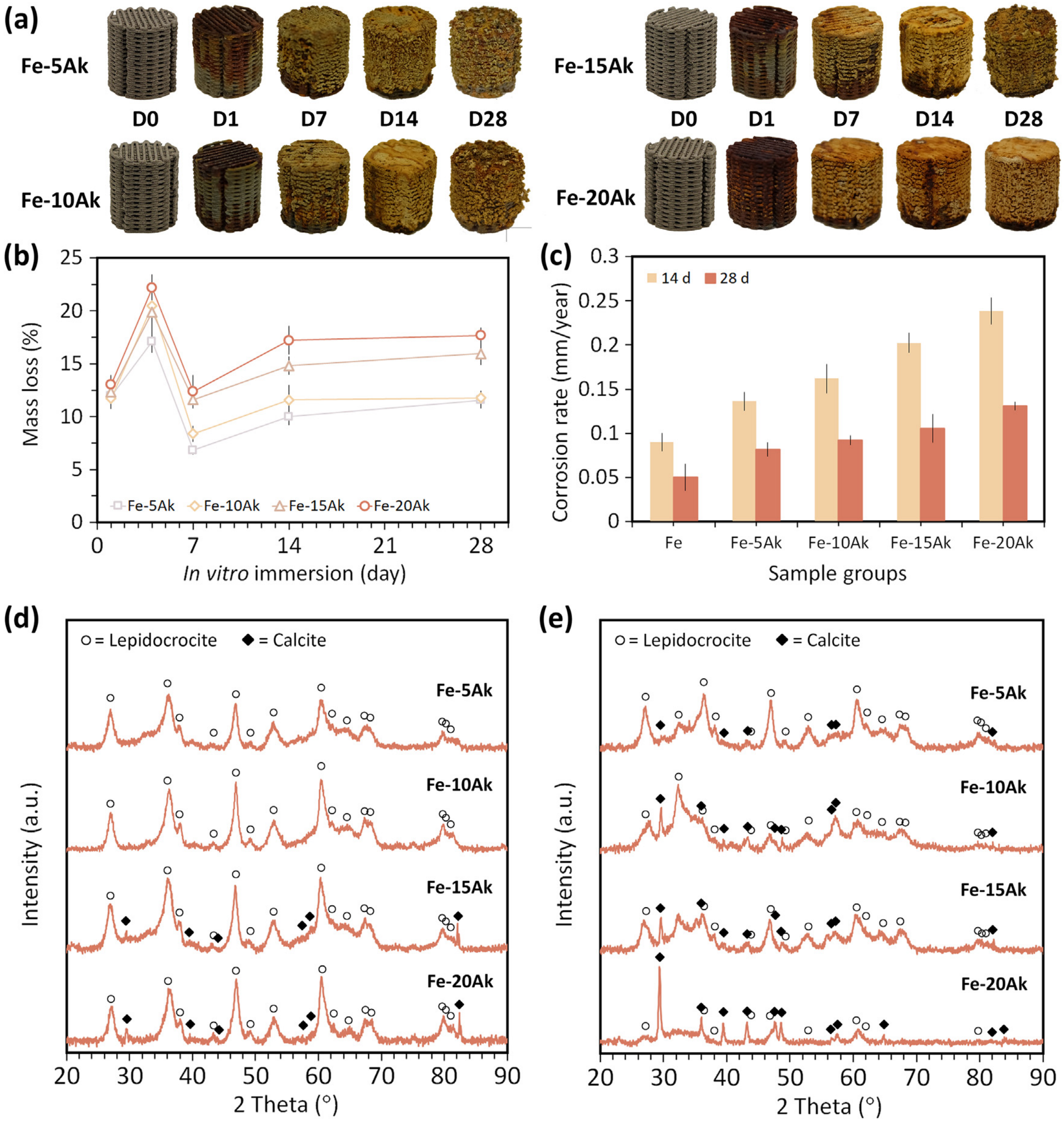

Fig. 3. The *in vitro* biodegradation characteristics of the porous iron-akermanite composites: (a) the visual inspection of the porous iron-akermanite composite scaffolds before and after biodegradation at various time points, (b) mass loss *vs.* immersion time, and (c) corrosion rates on days 14 and 28 of immersion, and the phase compositions of the biodegradation products on days (d) 4 and (e) 28 of immersion.

Table 2
Chemical compositions of the *in vitro* biodegradation products (wt%) on the periphery of the porous Fe-20Ak scaffolds, determined by EDS analysis.

Fe-20Ak	EDS point	C	O	Na	Mg	Si	Cl	P	Ca	Fe
4 d	**1**	36.35	19.94	–	0.46	0.36	–	–	0.94	41.95
	2	25.53	16.13	–	–	1.20	0.13	–	1.07	55.94
	3	24.25	9.41	–	–	–	–	–	–	68.70
	4	32.30	30.03	–	–	0.57	–	–	1.57	35.53
7 d	**5**	26.59	13.02	–	–	–	–	–	16.51	43.88
	6	25.11	19.03	–	0.59	0.16	–	4.02	7.52	43.56
	7	29.18	20.95	4.48	–	0.05	–	–	10.80	34.53
	8	18.41	33.73	–	–	0.19	–	–	25.32	22.35
14 D	**9**	30.68	23.24	0.07	1.15	–	–	–	19.77	25.09
	10	10.94	8.31	–	–	–	–	–	2.17	78.58
	11	4.46	1.58	–	0.66	–	–	–	18.27	75.02
	12	29.56	10.55	–	2.05	–	–	–	28.31	29.54
28 d	**13**	19.57	11.69	0.71	0.75	–	–	–	3.61	63.67
	14	31.88	7.78	0.31	0.54	–	–	–	26.51	32.98
	15	5.28	4.25	–	0.26	–	–	–	12.98	77.24
	16	20.20	14.30	–	1.18	–	–	–	46.69	17.82

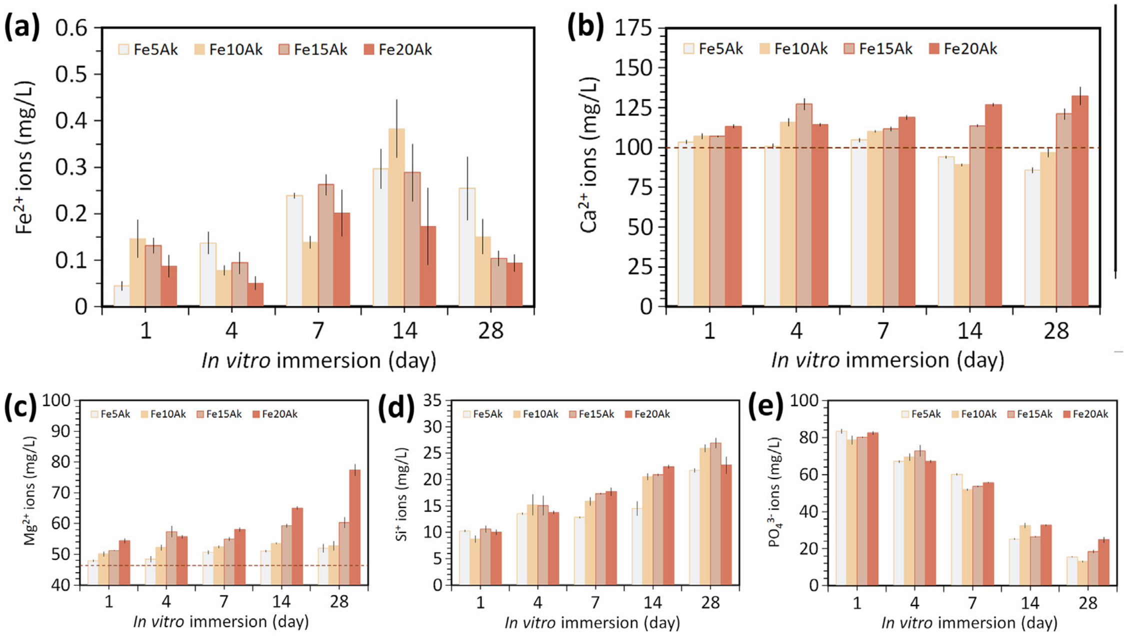

Fig. 4. The variations of the concentrations of the (a) Fe, (b) Ca, (c) Mg, (d) Si, and (e) PO_4 ions in the biodegradation medium over time. The dash line indicates the initial ion concentration values in the r-SBF medium.

In addition to the Fe- and Ca-based products, magnesium was detected at lower concentrations in the peripheral degradation products (Table 2**, S1–3**). Silicon was only present on the Fe-20Ak composite scaffolds at the early immersion time points (*i.e.*, 4 d and 7 d) (Table 2). Furthermore, the degradation products at the center of the scaffolds appeared to be compact. Moreover, Fe, C and O, Ca, Mg and Si remnants were found in the Fe-20Ak (Fig. 5m) and Fe-15Ak (**Figure S4m**) composite scaffolds. However, only Fe, C, O and Ca elements were observed in the cross-sectional biodegradation products of the Fe-10Ak (**Figure S5m**) and Fe-5Ak (**Figure S6m**) composites.

3.4. Electrochemical measurements

The iron-akermanite composite specimens (*i.e.*, Fe-5Ak, Fe-10Ak, Fe-15Ak and Fe-20Ak) showed relatively stable OCP values during the biodegradation experiments (Fig. 6a). At the beginning of the biodegradation experiments (*i.e.*, after 4 d), the OCP values were -645 ± 36 mV, -661 ± 21 mV, -693 ± 21 mV, and -669 ± 82 mV, respectively. At the 28th day of biodegradation, the average OCP values had only marginally increased to -645 ± 29 mV, -645 ± 19 mV, -670 ± 34 mV, and -602 ± 39 mV, respectively. The average polarization resistance (R_p) values of the porous iron-akermanite composites (*i.e.*, Fe-5Ak, Fe-10Ak, Fe-15Ak and Fe-20Ak) obtained from the LPR tests exhibited a generally decreasing trend as the biodegradation progressed (Fig. 6b). At day 4, the average R_p values were 9.0 ± 1.1 kΩ.cm^2, 8.3 ± 0.8 kΩ.cm^2, 6.9 ± 1.1 kΩ.cm^2, and 6.3 ± 1.6 kΩ.cm^2, respectively. After 28 d of biodegradation, the R_p values had decreased to 4.1 ± 0.8 kΩ.cm^2, 5.1 ± 1.1 kΩ.cm^2, 5.4 ± 1.4 kΩ.cm^2, and 3.9 ± 0.7 kΩ.cm^2, respectively.

The impedance modulus values of the porous iron-akermanite composites at low frequencies, indicative of the charge transfer and hence resistance of the corroding system, followed a decreasing trend with time similar to the R_p results (Bode plots - Fig. 6c-f). At a low frequency (*i.e.*, 0.01 Hz) and after 4 d of immersion, the impedance modulus values were 7.9 ± 1.8 kΩ.cm^2, 9.3 ± 0.9 kΩ.cm^2, 7.6 ± 1.8 kΩ.cm^2, and 10.7 ± 2.3 kΩ.cm^2, respectively, for Fe-5Ak, Fe-10Ak, Fe-15Ak, and Fe-20Ak. After 28 d of immersion, however, the impedance magnitude reduced to 3.7 ± 0.6 kΩ.cm^2, 4.8 ± 1.3 kΩ.cm^2, 5.1 ± 0.6 kΩ.cm^2, and 3.3 ± 0.6 kΩ.cm^2, respectively. The impedance magnitudes at a higher frequency (*e.g.*, 100 Hz) relate to the evolution (*e.g.*, partial dissolution or growth) of the corrosion product formation over time [70–72]. After 4 d of immersion, the impedance modulus values at 100 Hz were 0.4 ± 0.1 kΩ.cm^2, 0.5 ± 0.2 kΩ.cm^2, 0.3 ± 0.1 kΩ.cm^2, and 0.43 ± 0.03 kΩ.cm^2, respectively for Fe-5Ak, Fe-10Ak, Fe-15Ak, and Fe-20Ak. At the same frequency, the impedance modulus values after 28 d of immersion became 0.3 ± 0.1 kΩ.cm^2, 0.6 ± 0.3 kΩ.cm^2, 0.6 ± 0.1 kΩ.cm^2, and 0.35 ± 0.01 kΩ.cm^2, respectively. The peak start of the Bode plot phase angle at low-to-mid frequencies shows a trend to shift from a higher frequency to a lower frequency as a function of time of exposure (Fig. 6c-f). At a mid-frequency range (*i.e.*, 100 Hz), the phase angle values after 4 and 28 d of immersion for all composite scaffolds were relatively unchanged.

3.5. Mechanical properties

All the iron-akermanite composite scaffolds exhibited smooth stress-strain curves under uniaxial compression, starting with a linear elastic region and followed by a plastic deformation region that exhibited the hallmarks of strain hardening (Fig. 7a). The composite scaffolds (*i.e.*, Fe-5Ak, Fe-10Ak, Fe-15Ak and Fe-20Ak) had Young's moduli of 0.24 ± 0.03 GPa, 0.30 ± 0.01 GPa, 0.23 ± 0.05 GPa, and 0.17 ± 0.05 GPa, respectively. The yield strengths were 4.3 ± 0.3 MPa, 3.0 ± 0.1 MPa, 3.4 ± 0.5 MPa, and 2.9 ± 0.9 MPa, respectively. After 7 d of biodegradation, the Young's moduli of the scaffolds reduced to 0.20 ± 0.04 GPa, 0.19 ± 0.02 GPa, 0.12 ± 0.01 GPa and 0.10 ± 0.04 GPa, respectively (Fig. 7b). After 28 days of biodegradation, the Young's moduli improved from those measured at day 7 (*i.e.*, 0.23 ± 0.05 GPa, 0.30 ± 0.02 GPa, 0.17 ± 0.07 GPa and 0.13 ± 0.05 GPa, respectively), while being still lower than the initial values (Fig. 7b). The yield strengths of the specimens (*i.e.*, Fe-5Ak, Fe-10Ak, Fe-15Ak and Fe-20Ak) reduced to 3.4 ± 0.2 MPa, 2.25 ± 0.02 MPa, 1.5 ± 0.3 MPa, and 0.8 ± 0.2 MPa (Fig. 7c), respectively, after 28 d of biodegradation.

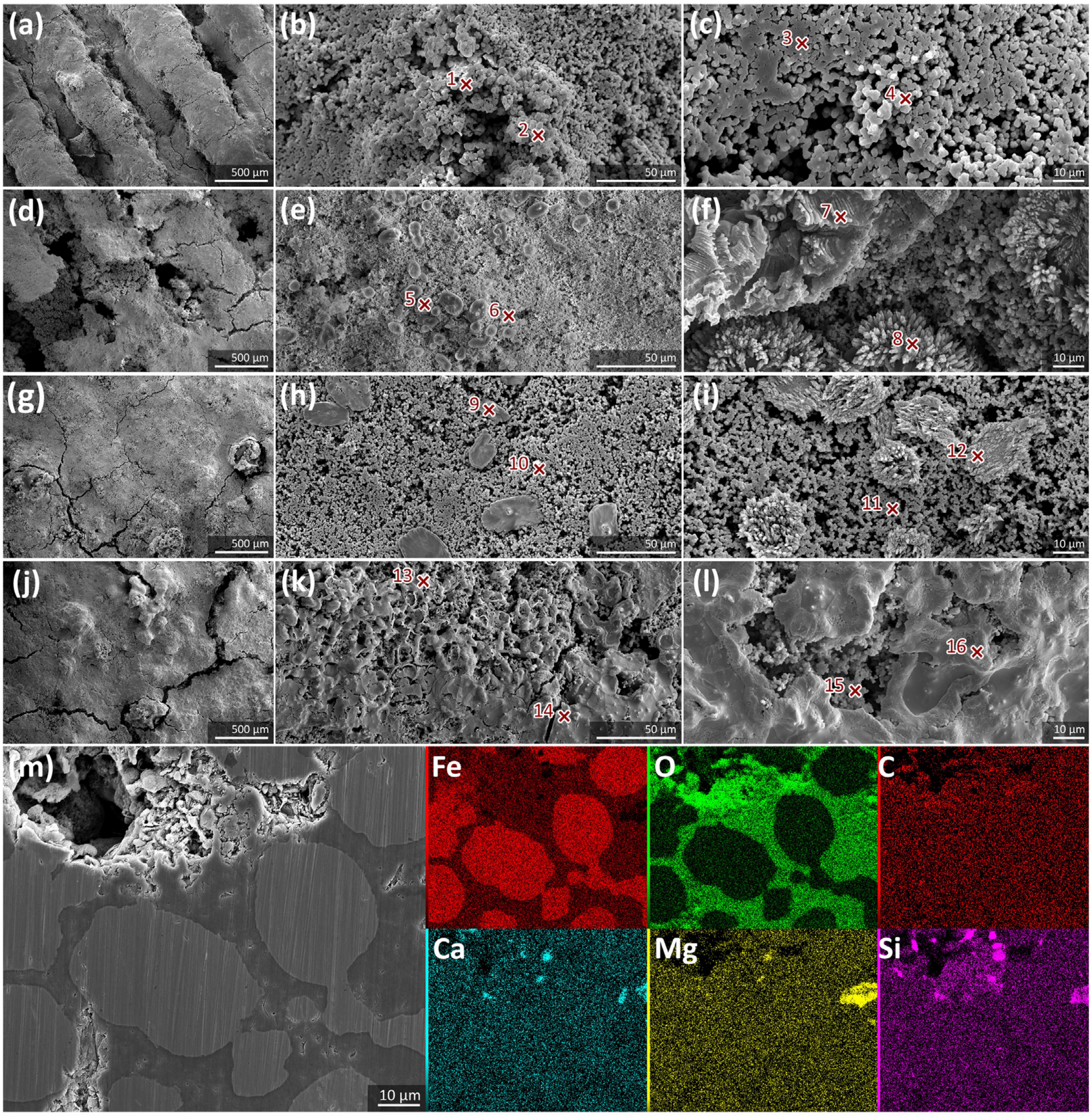

Fig. 5. The morphologies of the *in vitro* biodegradation products formed on the porous Fe-20Ak scaffolds: on the periphery after (a, b, c) 4 d, (d, e, f) 7 d, (g, h, i) 14 d, and (j, k, l) 28 d of biodegradation, and (m) at the center of the scaffolds after 28 d of biodegradation. The cross marks with numbers indicate the locations of the EDS analyses whose results are presented in Table 2.

3.6. *Metabolic activity of cells on the extracts of the composites*

For the 50% and 25% extracts, the preosteoblasts were highly metabolically active (*i.e.*, > 80%) for all the iron-akermanite specimens (Fig. 8a). When the extract concentration increased to 75%, the cells maintained their high levels of metabolic activity (*i.e.*, > 80%) for the Fe-10Ak, Fe-15Ak, and Fe-20Ak groups. These extracts were categorized as grade 1 (or non-cytotoxic) according to ISO 10,993-5 [73]. However, the metabolic activity of preosteoblasts dropped to < 50% when cultured in the 75% extracts of the Fe-5Ak composite (grade 2 or moderately reactive [73]). The inhibition of cell metabolic activity was only observed on all iron-akermanite extracts without any dilution (grade 4 or severely reactive [73]).

In the extracts of iron-akermanite, Ca^{2+} was the major component, followed by Si^{+} and Mg^{2+}, while the Fe^{2+} concentration was the lowest (Fig. 8b). The Ca^{2+} concentration was 78 ± 2 mg/L, 77 ± 3 mg/L, 67 ± 2 mg/L, and 62 ± 1 mg/L for the Fe-5Ak, Fe-10Ak, Fe-15Ak, and Fe-20Ak extracts, respectively. The Ca^{2+} concentration decreased as the volume fraction of the akermanite increased in the specimens. Likewise, the Fe^{2+} concentration values (*i.e.*, 21.7 ± 0.4 mg/L, 15 ± 2 mg/L, 12 ± 1 mg/L, and 12.2 ± 0.2 mg/L. respectively) were lower in the extracts of the specimens with higher akermanite volume fractions. The Mg^{2+} concentration was 26.8 ± 0.3 mg/L, 32 ± 1 mg/L, 36 ± 1 mg/L, and 43 ± 1 mg/L for the Fe-5Ak, Fe-10Ak, Fe-15Ak, and Fe-20Ak specimens, respectively. The corresponding values of the Si^{+} concentration were 44 ± 1 mg/L, 59 ± 2 mg/L, 60 ± 2 mg/L, and 66 ± 1 mg/L, respectively. Unlike Ca^{2+} and Fe^{2+}, higher concentrations of Mg^{2+} and Si^{+} were observed for the extracts of the specimens with higher volume fractions of akermanite.

3.7. *Proliferation of cells and their morphology on the composite scaffolds*

From day 7 of the cell culture, the preosteoblasts cultured on the porous Fe-10Ak, Fe-15Ak, and Fe-20Ak specimens showed significantly higher proliferation as compared to that of the Fe-5Ak specimens (Fig. 8c). A higher viable cell count was measured for

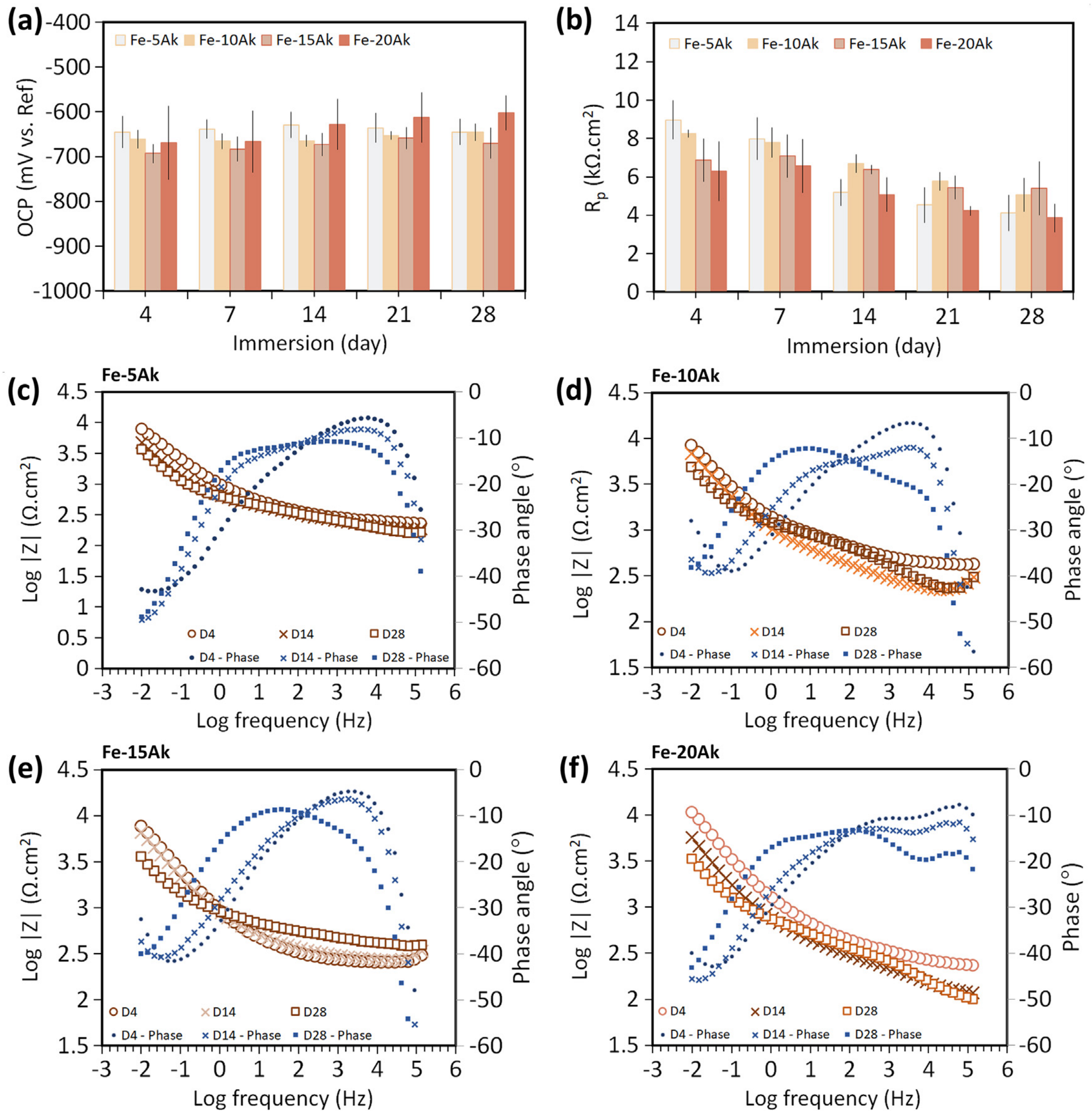

Fig. 6. The electrochemical measurements of the porous iron-akermanite composite scaffolds during 28 d of biodegradation: (a) OCP and (b) the R_p values from the LPR tests; Bode plot of (c) Fe-5Ak, (d) Fe-10Ak, (e) Fe-15k, and (f) Fe-20Ak composites, indicating the impedance modulus values at different frequencies at some selected time points after biodegradation.

the specimens with a higher volume fraction of akermanite. However, the preosteoblasts did not proliferate on the Fe-5Ak composite. In addition, a lower cell viability was observed, indicating that these specimens were cytotoxic. Therefore, this group was excluded from the osteogenic assays. At day 7 of cell culture, the numbers of preosteoblasts corresponding to the Fe-10Ak, Fe-15Ak, and Fe-20Ak specimens were not significantly different from the number of cells measured for the Ti-6Al-4 V specimens. At day 28 of cell culture, the cells grew more on Ti-6Al-4 V than on all the porous iron-akermanite scaffolds ($p < 0.0001$). Nevertheless, the number of preosteoblasts present on the composite scaffolds exhibited a 30-folds increase within the same period of time (Fig. 8c).

The fluorescent images revealed the morphologies and distributions of preosteoblasts after 7 d (Fig. 8d), 14 d (Fig. 8e), and 28 d (Fig. 8f) of culture on the porous Fe-10Ak, Fe-15Ak, and Fe-20Ak composites and Ti-6Al-4 V specimens. High-density, well-adherent cells were evident on the iron-akermanite composites with almost no differences from the cells residing to the Ti-6Al-4 V specimens, save for the Fe-5Ak scaffolds (**Figure S7**). On the SEM micrographs captured at days 7 (Fig. 9a) and 14 (Fig. 9b), the preosteoblasts were elongated and had developed extended poly-directional filopodia on the tested porous composite specimens (*i.e.*, Fe-10Ak, Fe-15Ak, and Fe-20Ak). By day 28, the preosteoblasts were integrated into fibrous matrix layers on the surface of the porous composite specimens (Fig. 9c). The preosteoblasts present on the Ti-6Al-4 V specimens proliferated well and formed multiple cellular layers by the end of the cell culture period. But such a fibrous-like layer was not observed on the Ti-6Al-4 V specimens. Preosteoblasts on the Fe-20Ak composite developed the densest fibrous matrix layer (Fig. 9d-e). On this matrix, the precipitation of minerals containing high Ca/P mass percentages, corresponding to the Ca/P atomic ratios in the range of 0.47 to 0.88 was identified (Table 3).

3.8. Collagen type-1 staining, Ca/P deposition, and ALP activity

Preosteoblasts cultured on the porous iron-akermanite composites demonstrated the initial cues of osteogenic differentiation. The fibrous matrix observed on the SEM micrographs (Fig. 9) was confirmed to be made of collagen type-1 (Fig. 10). At the 7th d of cell

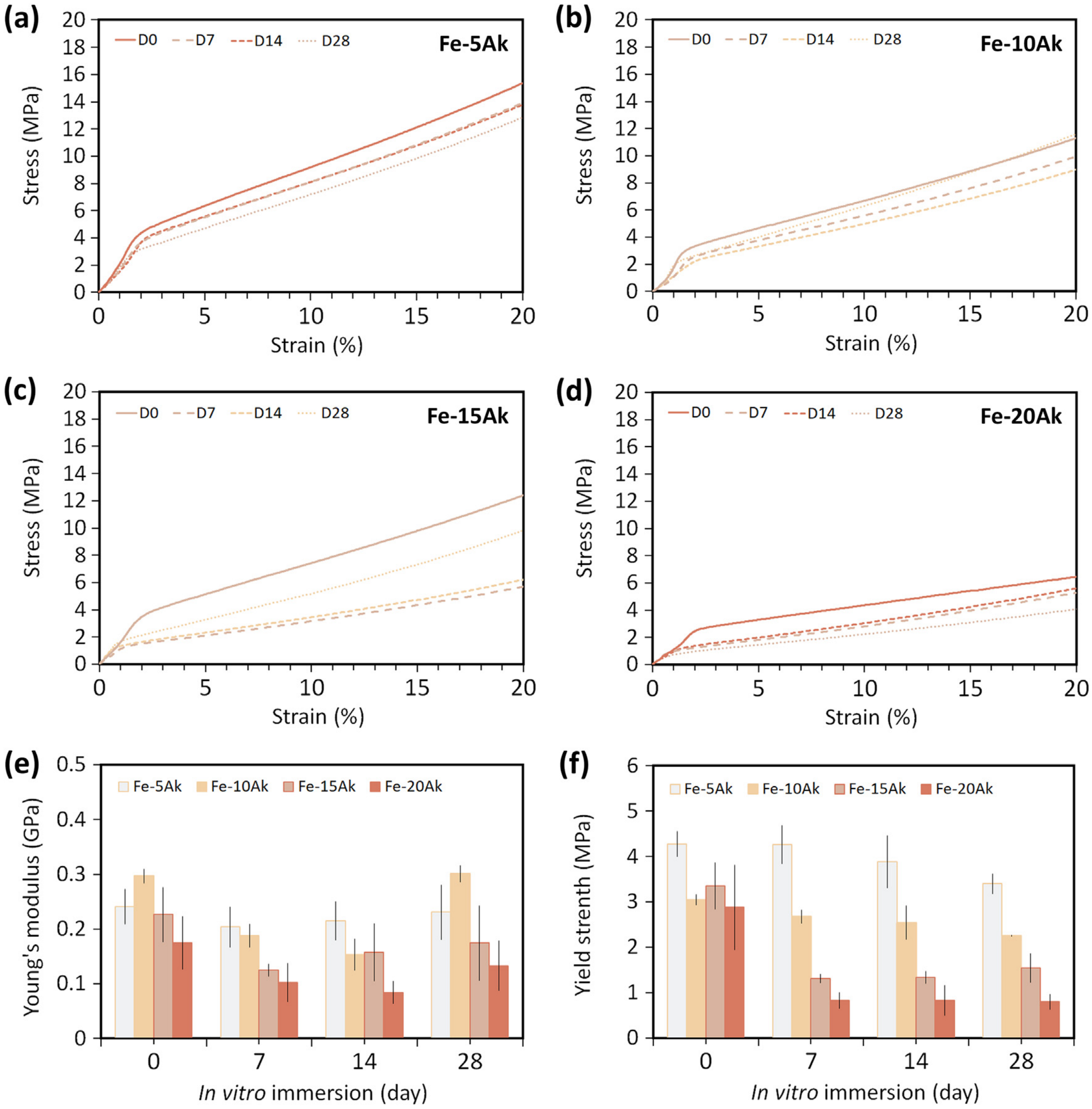

Fig. 7. The compressive mechanical properties of the porous iron-akermanite composites: the stress-strain curves of (a) Fe-5Ak, (b) Fe-10Ak, (c) Fe-15Ak, and (d) Fe-20Ak scaffolds; (b) changes in the Young's modulus and (c) yield strength during 28 d of biodegradation.

Table 3
Chemical compositions of the precipitated compounds (wt%) on the periphery of the porous Fe-Ak scaffolds after being cultured with preosteoblasts for 28 d, determined by EDS analysis.

EDS point		C	O	Na	Mg	Cl	P	K	Ca	Fe
Fe-10Ak	**1**	19.99	36.43	7.13	–	0.67	5.97	0.81	5.27	23.72
	2	14.34	27.62	6.57	–	0.97	9.57	1.14	7.68	32.11
Fe-15Ak	**3**	39.45	28.52	7.59	–	0.85	5.73	0.87	2.93	14.06
	4	32.63	28.57	6.04	–	–	8.30	0.75	3.90	19.81
Fe-20Ak	**5**	15.31	15.82	3.30	0.38	0.84	13.04	1.46	8.99	40.86
	6	16.24	16.45	5.02	–	0.85	12.72	1.98	8.29	38.45

culture, the collagen type-1 staining on the composites was more profound on the Fe-20Ak scaffolds than on the Fe-15Ak and Fe-10Ak scaffolds (Fig. 10a). The collagen type-1 matrix further intensified over 14 d of cell culture (Fig. 10b). At day 28, the matrix covered the struts of the Fe-15Ak and Fe-20Ak specimens (Fig. 10c). The porous iron-akermanite composites clearly induced more collagen secretion than the Ti-6Al-4 V specimens. In addition, the variation of the Ca^{2+} concentrations in the cell culture medium of the iron-akermanite composites with time was also measured (Fig. 10d). At day 7, the Ca^{2+} concentrations were 146.9 ± 5.3 mg/L, 155.6 ± 7.4 mg/L, and 169.4 ± 4.2 mg/L for the Fe-10Ak, Fe-15Ak, and Fe-20Ak groups, respectively. At days 14 and 28, the Ca^{2+} concentrations decreased to 127.0 ± 3.1 mg/L and 113.2 ± 6.8 mg/L for Fe-10Ak, 147.8 ± 2.4 mg/L and 97.0 ± 2.6 mg/L for Fe-15Ak, and 154.2 ± 4.2 mg/L and 104.9 ± 3.3 mg/L for Fe-20Ak.

Furthermore, at day 7, the ALP activity values of the preosteoblasts on the Fe-10Ak, Fe-15Ak, Fe-20Ak and Ti6Al4V specimens were 1.0-fold, 1.1-fold, 1.1-fold, and 2.6-fold higher than the negative control groups, respectively. At day 14, the ALP activity values were 1.5-fold, 1.3-fold, 1.7-fold, and 2.9-fold higher than the

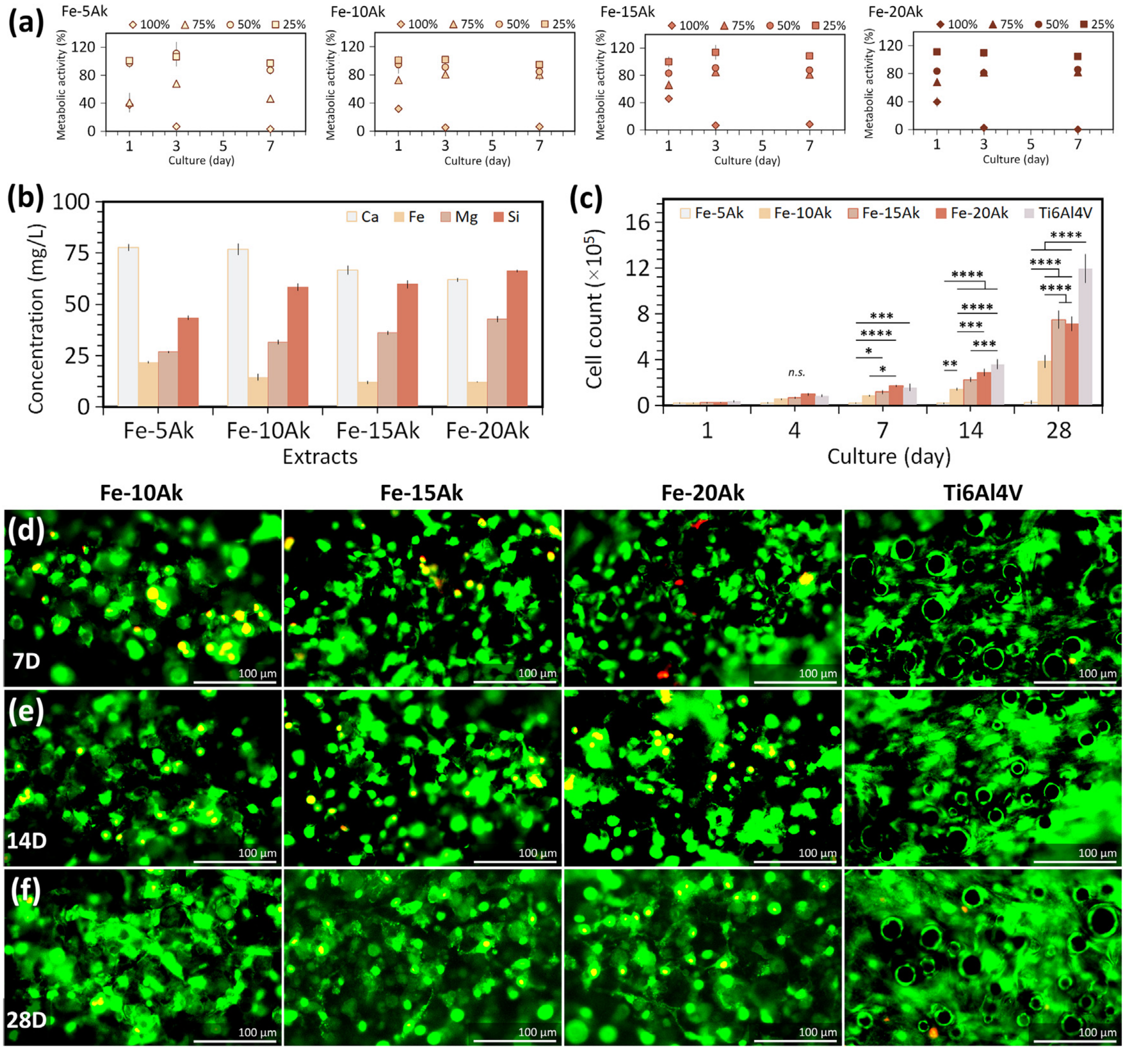

Fig. 8. The compatibility of the porous iron-akermanite composites with the MC3T3-E1 preosteoblasts: (a) the metabolic activity of the preosteoblasts after culture with the extracts of the porous iron-akermanite composites, (b) The concentrations of the Ca, Fe, Mg, and Si ions in the iron-akermanite extracts, (c) the number of the cell counts over the 28 d of culture, and the live dead staining of the preosteoblasts on the porous Fe-10Ak, Fe-15Ak, and Fe-20Ak and Ti-6Al-4 V scaffolds after (d) 7 d, (e) 14 d, and (f) 28 d of culture. $^{****} = p < 0.0001$, $^{***} = p < 0.001$, $^{**} = p < 0.01$, and $^{*} = p < 0.05$.

negative control groups, respectively. At day 28, the ALP activity values of the preosteoblasts cultured on the composite specimens (*i.e.*, Fe-10Ak, Fe-15Ak, Fe-20Ak) were 2.4-fold, 2.5-fold, and 2.3-fold higher than the negative control groups. The values were almost comparable to the Ti-6Al-4 V specimens cultured in the osteogenic medium (*i.e.*, 2.5-fold higher than the negative control groups).

4. Discussion

The results of this study show the potential of iron-akermanite composite scaffolds fabricated using extrusion-based 3D printing for enhancing the performance of iron-based bone substitutes. The developed biomaterials successfully addressed both challenges associated with iron-based bone substitutes, namely their low rates of biodegradation and limited bioactivity. The biodegradation rates (*i.e.*, 0.08–0.13 mm/y 28 d *in vitro*) were significantly enhanced due to the addition of 5–20 vol% akermanite to iron. Despite the intensified biodegradation, the porous composites maintained their mechanical properties (*i.e.*, E = 0.13–0.24 GPa and σ_y = 0.8–4.3 MPa) high enough to be in the range of the values reported for the cancellous bone [74]. Furthermore, the composite scaffolds provided a favorable environment for the adhesion, proliferation, and osteogenic differentiation of preosteoblasts. These findings further advance the development of additively manufactured porous biodegradable iron for application as bone substitutes, encouraging further *in vivo* research to bring them closer to clinical applications.

4.1. Extrusion-based 3D printing of the porous iron-akermanite scaffolds

Extrusion-based 3D printing, followed by debinding and sintering, accomplished the additive manufacturing of porous iron-akermanite composite scaffolds. We created iron-akermanite-containing inks that could be simply extruded into 3D porous architecture at ambient temperature. Here, the choice of binder is of critical importance, *e.g.*, hypromellose polymer (**Figure S2**) being able to provide the inks with the shear-thinning properties that are required to enable smooth flow without clogging the nozzle tip [75–78]. The printing pressure was the only variable that was altered during the 3D printing of the inks. A higher printing pressure was required for a more viscous iron-akermanite ink (**Figure S2**). The viscosity values of the inks differed due to the hydrophilic behavior of akermanite [79], which increased with the volume fraction of akermanite suspended in the ink. Upon extru-

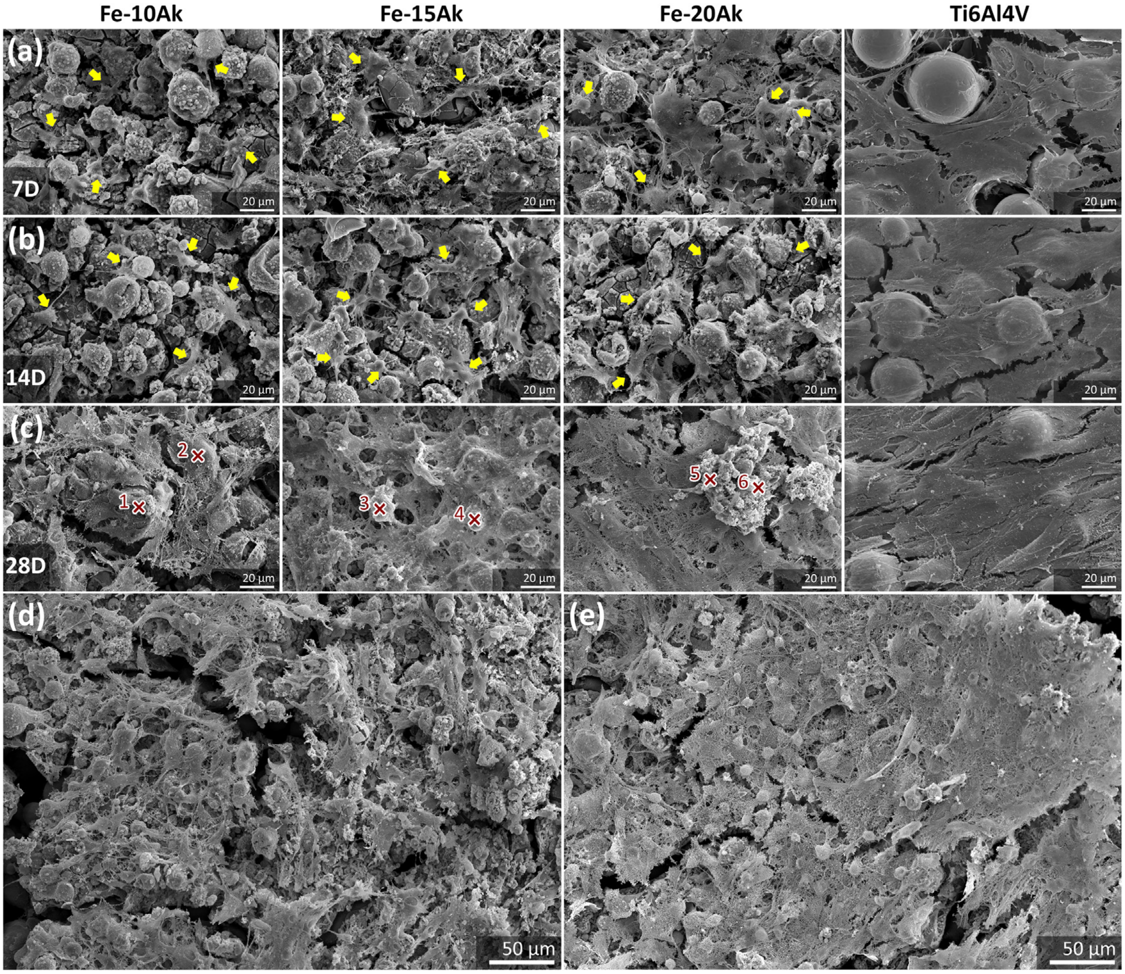

Fig. 9. The morphologies of the preosteoblasts after (a) 7 d, (b) 14 d, and (c) 28 d of culture on the Fe-10Ak, Fe-15Ak, and Fe-20Ak composite scaffolds. At a lower magnification, the formation of fibrous extracellular matrix on the periphery of the (d) Fe-10Ak and (e) Fe-20Ak composites.

sion, the inks quickly solidified, meaning that the shape of the scaffolds could be well maintained. The green-bodies were robust (**Figure S1**) and could be immediately transformed into porous iron-akermanite composites through the debinding and sintering process steps (Fig. 1).

The composite scaffolds contained well-defined macro pores that conformed to the original design (Fig. 1d). The choice of the sintering parameters (*i.e.*, temperature = 1200 °C and time = 6 h) allowed iron and akermanite powder particles to be partially sintered, resulting in minimal shrinkage. The partially sintered iron-akermanite powders provided random micro pores in the struts (Fig. 1e-h), thereby increasing the total porosity of the final scaffolds beyond the initially designed values (with solid struts). Iron particles appeared to have been coated with Ca, Mg, and Si (Fig. 1i), which was due to the water-based binder in the ink that promoted the dissolution of akermanite particles during the ink preparation and the 3D printing processes (**Figure S3**). This coating could be beneficial for the adhesion and proliferation of osteoprogenitor cells to promote osseointegration [23,80]. The iron-akermanite composite scaffolds exhibited a large pore interconnectivity (*i.e.*, 97–99%, Fig. 2a). A highly interconnected porous scaffold has been suggested to be beneficial for tissue regeneration [81], as it allows for improved cell migration, nutrition, and oxygenation throughout the scaffolds.

Furthermore, the composite scaffolds only contained the α-Fe and akermanite phases (Fig. 2c), indicating that the two materials maintained their individual characteristics even after exposure to the high temperature during sintering at 1200 °C for 6 h. However, at the interfaces, iron had diffused into the akermanite phase (Fig. 2d). Such an event has been also observed in other studies on iron-based composites prepared by using the sintering technique [44,46,47]. Proper interfacial bonding between both material types is of importance, as poorly bonded interfaces often cause premature failure when applied stress exceeds certain thresholds [82–84]. Such interface diffusion between the iron matrix and the akermanite phase may strengthen the mechanical integrity of the composite scaffold for its intended use and assist with the bone regeneration process.

4.2. Biodegradation

Porous iron-akermanite composites demonstrated significant increases in their rates of *in vitro* biodegradation (*i.e.*, from 1.6 to 2.6 times at day 28) as compared to porous monolithic iron scaffolds [37]. The higher solubility of akermanite in the physiological solution (as compared to iron) led to a higher mass loss during the initial 4 days of biodegradation for all the scaffolds (Fig. 3b), which is in line with the biodegradation mechanisms of typical iron-bioceramic composites described in the literature [40,46,47]. The mass loss values dropped on day 7 and progressed with even lower rates for the later time points (*i.e.*, days 14 and 28) of the biodegradation tests. Such variations in mass loss were a result of the precipitated biodegradation products that influenced the corrosion process. Indeed, the addition of akermanite enhanced the

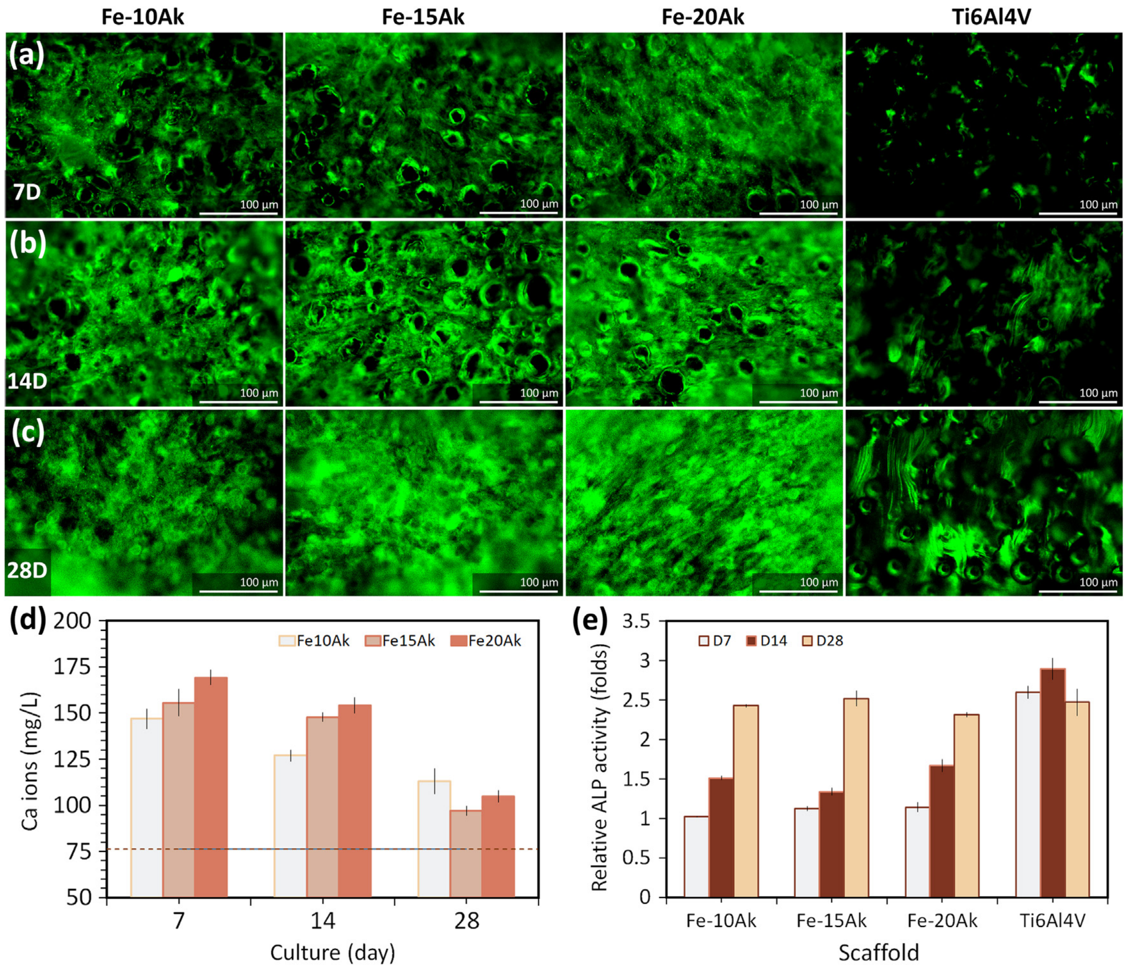

Fig. 10. Collagen type-1 staining on the porous Fe-10Ak, Fe-15Ak, and Fe-20Ak composite scaffolds after culture with preosteoblasts for (a) 7 d, (b) 14 d, and (c) 28 d (d) The variations of the Ca ion concentration in the cell culture medium during the cell culture period. (e) The ALP activity values of the preosteoblasts at a number of selected time points.

biodegradation of the composites. This was further confirmed by the continuous release of Ca^{2+}, Mg^{2+}, and Si^{+} into the immersion medium (Fig. 4). Besides its favorable solubility, the dissolution of akermanite is expected to have also created available microchannels for r-SBF to be in contact with more iron surfaces for biodegradation.

As corrosion naturally occurred during the immersion tests, the degradation products precipitated all over the surfaces of the composite scaffolds (Fig. 5, **S4–6**). In general, the dense Fe-based corrosion products are known to promote the passivation of the substrate, thereby slowing down biodegradation at the later time points of the immersion period (Fig. 3c). The principal phase in the degradation products was identified to be γ-FeOOH (Fig. 3d-e). This is similar to other biodegraded Fe scaffolds [22].

Ca-based biodegradation products were also identified. The precipitation of Ca-based degradation products can be related to the total Ca^{2+} concentration in the immersion medium (Fig. 4). The concentration of Ca^{2+} released from akermanite into SBF was reported to be approximately 5 times higher than its initial concentration in the medium after 20 days of *in vitro* biodegradation [85]. After 28 d of biodegradation, however, the Ca^{2+} concentrations in the immersion media of the Fe-15Ak and Fe-20Ak specimens were only 1.2–1.3 times higher than the initial concentration in the r-SBF medium (Fig. 4b). For the specimens with a lower akermanite volume fraction (*i.e.*, Fe-5Ak or Fe-10Ak), Ca^{2+} released from the akermanite phase was merely sufficient to maintain the ion concentration close to the original value in r-SBF for 7 days. At the later time points of immersion, the Ca^{2+} concentration even dropped (Fig. 4b). These imply that the Ca^{2+} released from the composite scaffolds mostly participated in the formation of the biodegradation products. However, the expected calcium phosphate compounds were not detected, despite the significant decline in the concentration of the PO_4^{3-} in the immersion medium (Fig. 4e). The P element was scarcely observed in the other biodegradation products (Table 2**, S1–3**). Instead, $CaCO_3$ formed on the composite scaffolds as early as day 4 of the immersion test (Fig. 3d-e). This is likely because the biodegradation process took place in a 5% CO_2 atmosphere, which maintained the HCO_3^- concentration in the immersion medium, allowing $CaCO_3$ to form [86].

The $CaCO_3$ phase is stable in the presence of Mg and Si [87–89]. Given that we observed the $CaCO_3$ phase in the biodegradation products up to the end of the immersion test period (*i.e.*, 28 d), the stabilization stage must have occurred due to the readily accessible Mg^{2+} and Si^{+} in the immersion medium (Fig. 4c-d). The Mg^{2+} and Si^{+} concentrations continuously increased over the immersion period (Fig. 4c-d). The Mg-based biodegradation products (*e.g.*, $Mg(OH)_2$) are known to be stable in environments with pH $\geq$ 11.5 [90]. The absence of Mg- or Si-based biodegradation products is, therefore, not unexpected, given that the biodegradation takes place under relatively stable pH conditions with a pH value of up to 7.65. In addition, for calcium phosphate formation in CaO-SiO_2-based compounds, such as akermanite, a negatively charged

Table 4

Biodegradation rates of extrusion-based 3D printed iron-akermanite composites during *in vitro* immersion tests in comparison to the values reported in the literature.

Material and fabrication technique		Porosity (%)	Immersion condition	Time points	Biodegradation rate (mm/year)	Ref.
Porous Fe-Ak	Extrusion-based 3D printing and sintering	70–72	Static, 37 °C 5% CO_2 r-SBF	14 d	0.14 – 0.24, or 2.9 – 5.1*	This study
				28 d	0.08 – 0.13, or 1.8 – 2.8*	
Fe-30TCP(vol%) **Fe-40TCP (vol%)** **Fe-50TCP (vol%)**	Powder injection molding	–	Static, 37 °C 0.9% NaCl	56 d	0.2 0.196 0.150	[43]
Fe-5HA (wt%) **Fe-5TCP (wt%)** **Fe-5BCP (wt%)**	Powder metallurgy and sintering	–	Static, 37 °C Kokubo's solution	14 d	1.01* 1.49* 2.16*	[40]
Fe-1.5Mg_2Si (wt%)	Powder metallurgy, ball milling, and sintering	0.9–2.1	Static, 37 °C 5% CO_2 Hank's modified solution	14 d	0.19 – 0.28	[48]
Fe-20$CaSiO_3$ (wt%) **Fe-30$CaSiO_3$ (wt%)** **Fe-40$CaSiO_3$ (wt%)**	Powder metallurgy and sintering	–	Static, 37 °C SBF	28 d	∼1.7* ∼2.3* ∼3.3*	[46]
Porous Fe-30$CaSiO_3$ (wt%)	3D printing and sintering	n/a	Static, 37 °C Tris–HCl	28 d	∼12**	[29]
Fe-25TCP (vol%) **Fe-50TCP (vol%)**	Powder metallurgy and sintering	–	Static, 37 °C 0.9% NaCl	12 w	0.12	[45]
Fe-5Bredigite (wt%) **Fe-7.5Bredigite (wt%)**	Selective laser melting	–	Static, 37 °C SBF	14 d	4.5* 5.9*	[51]

The values were expressed in *g/m^2/d and ** percentage of mass loss.

surface made of a hydrated silica-rich layer is required for apatite nucleation [85]. The unavailability of Si-based biodegradation products can further explain the delay in the growth of bony apatite on the struts of the scaffolds. A favorable property of the $CaCO_3$ phase is that it is a precursor material for the carbonate apatite mineral [91–93]. $CaCO_3$ is well-known for its biodegradability and bioactivity and is clinically used as a bone filler [94]. The addition of $CaCO_3$ to the biodegradation products is, therefore, expected to improve the cytocompatibility of the developed bone substitutes.

The precipitation of the biodegradation products influences the electrochemical responses of the specimens. The stable OCP values (Fig. 6a) suggest that the iron-akermanite composite scaffolds preserved their susceptibility to biodegradation over time and that their associated biodegradation products did not passivate the base materials (Fig. 6b). The modulus of the impedance at low frequencies, indicative of the charge transfer and hence corrosion resistance, shows a reducing trend with time (Fig. 6c-f), which is similar to the R_p results (Fig. 6b). In addition, the impedance modulus values at mid-frequency range (*e.g.*, 100 Hz), indicative of the evolution of the corrosion products [70–72], were relatively stable over time (Fig. 6c-f) albeit that some ongoing corrosion product formation is suggested by the trend of the peak start of the Bode plot phase angle at low-to-mid frequencies to shift from a higher frequency to a lower frequency as a function of time of exposure [95]. All in all, the EIS data analysis indicates that the intrinsic integrity and protectiveness of the biodegradation products is relatively limited. The decreasing resistivity and the evolution of the corrosion process can also be explained by the formation and maturation of $CaCO_3$ on the surfaces of the specimen struts. Despite its dense coverage on the surfaces, the biodegradability of $CaCO_3$ [94] means that corrosion can continuously progress into the base materials.

In general, the *in vitro* biodegradation rates of the iron-akermanite composite scaffolds are comparable with those reported in the literature (Table 4). However, the Fe-based composites were mostly studied in the bulk form and contained different types or compositions of bioceramics, which makes a direct comparison challenging. Several factors are of importance to consider when one compares the biodegradation rates of Fe-based composites. Firstly, the addition of bioceramics with a high-volume fraction to the Fe matrix improves the biodegradability of the composites. For example, akermanite biodegraded faster than TCP [59,61], but the bulk Fe composites with higher TCP volume fractions (*i.e.*, 25–50 vol% [43,45]) biodegraded more rapidly than our composite scaffolds with lower akermanite volume fractions (*i.e.*, 5–20 vol%). Secondly, bioceramics are often selected based on their own biodegradation profiles. For example, bredigite has a higher biodegradation rate than akermanite [96]. The addition of 5 and 7.5 wt% bredigite to the Fe matrix [51] led to much higher rates of biodegradation than our scaffolds made of Fe-15Ak (= 6.2 wt% Ak) and Fe-20Ak (= 8.6 wt% Ak). However, this can be further tuned by the design of the composite structure (*e.g.*, open porosity or intricate porous design). For instance, $CaSiO_3$ is known for its superior biodegradability [61,97], but the bulk Fe-based composites containing 20–30 wt% $CaSiO_3$ did not biodegrade faster, as compared to porous Fe-20Ak (= 8.6 wt% Ak) composite scaffolds [46,47]. The high interconnected porosity of the iron-akermanite composite scaffolds clearly enhances their biodegradation rates, even though the dissolution rate of akermanite is lower than that of $CaSiO_3$ [61].

In addition, the fabrication processes applied to a composite material can alter its biodegradation profile too. A powder metallurgy technique that includes ball milling can create a much-refined microstructure of the resulting powder particles, which often results in an enhanced biodegradation rate of the composite. The bulk Fe composite containing 5 wt% HA did not show a faster biodegradation rate compared to the bulk pure Fe [40]. When the HA particles were milled into various smaller sizes, the biodegradation rate of Fe-5 wt% HA composites increased up to 5 times [42]. Similar event was also reported for the Fe-Mg_2Si composites [48–50] given in Table 4.

Furthermore, the immersion solution influences the biodegradation rates. We used the r-SBF medium that has the same ion concentrations as the blood plasma. Other available solutions (*e.g.*, SBF or modified Hank's Balanced Salts) contain a higher concentration of Cl^- that can accelerate the biodegradation of iron. Moreover, the addition of proteins to the solution has been reported to affect the corrosion profile of iron [98]. Finally, and most importantly, the corrosion profile of Fe-based composites should be styled for sustainable biodegradation, while maintaining the mechanical integrity of the bone substitutes.

4.3. Mechanical behavior

When loading is applied to a composite scaffold, the load will be transferred from the iron matrix to the reinforcing phase across many interfaces [39]. Therefore, good interfacial bonding between iron and akermanite is of importance to ensure that high strength is achieved and the mechanical integrity of the composite material is preserved. Our iron-akermanite composite scaffolds were capable of maintaining their mechanical properties (*i.e.*, $E = 0.13$–0.24 GPa and $\sigma_y = 0.8$–4.3 MPa) in the range of those of the cancellous bone [74], even after 28 days of biodegradation and did not exhibit any signs of premature failure (Fig. 7). The addition of 10 vol% akermanite to the iron matrix led to the highest Young's modulus value (Fig. 7b). As for the yield strength, adding akermanite did not improve the value. The mechanical properties of the composite scaffolds were much lower than those of the porous monolithic iron ($E = 0.6$ GPa and $\sigma_y = 7.2$ MPa) [37]. This could be attributed to the intrinsically brittle nature of akermanite and its low fracture toughness [99].

Biodegradation usually reduces the mechanical properties of the biomaterials. The change in the mechanical properties should be tailored to match the rate of bone tissue regeneration to ensure that the required mechanical support continues to be available. The yield strength decreased with biodegradation time for all the porous iron-akermanite scaffolds. Similar trends have been also observed for Fe-TCP composites (with 30–40 vol% TCP) after 56 days of biodegradation [43]. Interestingly, the Young's moduli of the composite scaffolds increased at the later time points of biodegradation (Fig. 7b-c).

The changes in the mechanical properties can be explained by the interactions between the composite scaffold and its biodegradation products during mechanical loading. The bonding between the biodegradation products and the strut surfaces and pores of the composite scaffolds is due to the van der Waals forces. When subjected to small levels of compressive strain, this weak bonding can share the load between the composite matrix and the degradation products, hence increasing Young's modulus. The improvement in Young's modulus after biodegradation is likely due to the strengthening effect of precipitation and the growth of the biodegradation product phases and has been observed in other studies as well [100,101]. At the higher levels of strain (*e.g.*, reaching the yield strain), however, such load transfer will fail. From there on, the mechanical strength will only depend on the biodegraded base materials, which is why the yield strength decreases with immersion time. It is important to note that the inclusion of up to 20 vol% akermanite in the composite did not make the composite material brittle. The iron-akermanite scaffolds exhibited a ductile behavior despite biodegradation (Fig. 7), which is important for enduring cyclic loading when used as load-bearing bone substitutes.

4.4. Cytocompatibility and osteogenic properties

Limited bioactivity is one of the major challenges hampering the clinical use of biodegradable Fe-based materials. The response of the cells to biodegradable materials is strongly conditioned by the concentrations of the ions released into the medium and the formation of the biodegradation products. In the present work, the iron-akermanite composite scaffolds (with 10–20 vol% akermanite) received a high metabolic response from the preosteoblasts MC3T3-E1 cell line (Fig. 8). The composite scaffolds were favored by the cells for adhesion and proliferation over the entire period of the cell culture experiments (Fig. 8). The specimens also allowed the deposition of collagen type-1 (Fig. 9) and the formation of initial bone minerals *in vitro* (Fig. 10).

First, we evaluated the metabolic activity of preosteoblasts using the iron-akermanite extracts. A higher volume fraction of akermanite in the composite scaffold resulted in lower concentrations of Ca^{2+} and Fe^{2+} released into the medium (Fig. 8b). The reduced Ca^{2+}concentration in the extracts corresponded to the formation of Ca/P compounds on the composite scaffolds during the immersion in the cell culture medium (**Figure S8, Table S4**). The Fe^{2+} depletion could be due to its precipitation in the formation of other degradation products (*e.g.*, made of carbonates). The cytocompatibility of the Fe-based composite scaffolds is mainly limited by the high concentration of released Fe^{2+}, which catalyzes the formation of radical compounds that are harmful to cells [102]. However, the Fe^{2+}concentration values in all the extracts were much lower than the inhibitory concentration (IC_{50}) reported for preosteoblasts [38]. This implies that the inhibition of the metabolic activity by 100% extracts may be due to other factors, such as the highly ionic environment in the medium which could induce cell death [103]. With a slight dilution (*i.e.*, 1.3 ×), the preosteoblasts turned highly active in the Fe-10Ak, Fe-15Ak and Fe-20Ak extracts. These results were very much improved compared to those of monolithic iron scaffolds [37].

Furthermore, we studied the adhesion, proliferation, and osteogenic differentiation of the preosteoblasts directly cultured on the composite scaffolds with a high medium amount to minimize the local build-up of metal ions and better mimic the *in vivo* conditions (*e.g.*, in the presence of *in vivo* fluid circulation). The Fe-5Ak composite scaffold was found to exhibit a similar cytotoxic response to the pure iron scaffold (as reported elsewhere [37]). The Fe-5Ak group released a higher concentration of Fe^{2+}, as compared to the other composite scaffold groups (Fig. 8b), which must have contributed to the cytotoxicity of the material. In other words, the 95 vol% iron content in the composite appeared to be still too high to provide a cytocompatible and bioactive environment for the cells. Conversely, the preosteoblasts were viable and proliferated on the Fe-10Ak, Fe-15Ak, and Fe-20Ak composites (Fig. 8c). The proliferation rates of the cells cultured with the composite scaffolds (with 10 – 20 vol% Akermanite) were comparable to the values measured for Ti-6Al-4 V (the reference) during the first 7 days but somewhat decreased over time. Nevertheless, the preosteoblasts were actively growing over time (Fig. 8c), which is a strong indicator for the cytocompatibility of the Fe-based composite scaffolds for these cells. In addition, the preosteoblasts well adhered to the composite surfaces (Fig. 8d-f) with an elongated shape and poly-directional filopodia (Fig. 9a-b). Despite the enhanced biodegradation rates, all the hallmarks of cytocompatibility were observed in the response of the preosteoblasts to the composite scaffolds. This is caused by the addition of akermanite to the Fe matrix [59–61]. Similar levels of cytocompatibility have been also observed for other types of Fe-based composites (*e.g.*, Fe-TCP [40], Fe-$CaSiO_3$ [46,47], and Fe-Bredigite [51]).

The composite scaffolds (containing 10–20 vol% akermanite) further evidenced their ability to induce osteogenic differentiation without the use of any osteogenic reagent (*i.e.*, ascorbic acid or β-glycerophosphate) during the cell culture experiments. At the later time points (*i.e.*, from 7 d onwards), the preosteoblasts secreted a fibrous-like matrix (Fig. 9) that was recognized as collagen type-1 (Fig. 10a-c). Collagen substrate has been shown to facilitate the precipitation of minerals and support osteogenic differentiation [104,105]. We observed high amounts of Ca/P elements (Table 3) in the minerals deposited on the collagen layer (Fig. 9c) along with other molecules (*e.g.*, carbonate-based precipitates). On the contrary, the formation of Ca/P compounds on the scaffolds immersed in the cell culture medium without cells (**Figure S8, Table S4**) only occurred on the surfaces of akermanite particles, but not on Fe particles. Finally, the composite scaffolds enhanced the ALP activity of the cells from day 14 towards a level comparable with that of the cells cultured on Ti-6Al-4 V scaffolds under the osteogenic conditions at day 28 (Fig. 10e). Akermanite was previously found to promote the osteogenic differentiation rat bone marrow stem cells [60] and of human bone marrow stem cells [106] even without any need for osteogenic supplements [107]. Taken together, our *in vitro* results show the potential of the iron-akermanite composite scaffolds as osteoinductive biomaterials to assist bone regeneration.

5. Conclusions

We used extrusion-based 3D printing to fabricate, for the first time ever, porous iron-akermanite composite scaffolds. We then studied the characteristics of the porous composite scaffolds, aiming to bring Fe-based biomaterials closer to meeting the clinical requirements for bone substitution. The fabricated composites possessed a highly interconnected porous structure. The *in vitro* biodegradation rates of the composite scaffolds were enhanced due to the presence of akermanite in the α-Fe matrix. The biodegradation process and its associated product formation on the composite scaffolds influenced the mechanical properties of the composites. However, the yield strengths and elastic moduli of the specimens stayed in the range of those reported for the cancellous bone even after 28 days of biodegradation. Indirect cell culture showed the enhanced cytocompatibility of the composites for preosteoblasts as compared to similarly processed pure iron, which was most likely caused by the presence of Ca^{2+}, Mg^{2+}, and Si^{+} in the culture medium. In direct cell cultures, the preosteoblasts well-adhered to the composite specimens (containing 10–20 vol% akermanite), proliferated over time, and secreted the collagen type-1 matrix that stimulated bony-like mineralization. In terms of ALP activity, the composite specimens (containing 10–20 vol% akermanite) were not significantly different from the positive control (*i.e.*, Ti6Al4V specimens), when subjected to the cell culture under osteogenic conditions. Taken together, the results of this study clearly show the exceptional potential of the developed porous composite scaffolds for application as bone substitutes and motivate further research into their *in vivo* performance.

Declaration of Competing Interest

The authors declare that they have no known competing financial interests or personal relationships that could have appeared to influence the work reported in this paper.

Acknowledgments

This work is part of the 3DMed project that has received the funding from the Interreg 2 Seas program 2014 – 2020, co-funded by the European Regional Development Fund under subsidy contract No. 2S04–014. Karl G.N. Borg thank the Tertiary Education Scholarships Scheme (TESS) from the Ministry for Education and Employment, Malta. The authors acknowledge the participation from Dutch Medical Delta project: RegMed4D. The authors acknowledge Mr. Michel van den Brink at the Department of Process and Energy, Delft University of Technology for ICP-OES analysis. The authors acknowledge Mr. Ruud Hendrikx at the Department of Materials Science and Engineering, Delft University of Technology for XRD analysis. The authors thank Mrs. Agnieszka Kooijman at the Department of Materials Science and Engineering, Delft University of Technology for her assistance in the electrochemical experiments.

Supplementary materials

Supplementary material associated with this article can be found, in the online version, at doi:10.1016/j.actbio.2022.06.009.

References

[1] Y.F. Zheng, X.N. Gu, F. Witte, Biodegradable metals, Mater. Sci. Eng. R 77 (2014) 1–34, doi:10.1016/j.mser.2014.01.001.

[2] J. He, F.L. He, D.W. Li, Y.L. Liu, Y.Y. Liu, Y.J. Ye, D.C. Yin, Advances in Fe-based biodegradable metallic materials, RSC Adv. 6 (2016) 112819–112838, doi:10.1039/C6RA20594A.

[3] H. Hermawan, Updates on the research and development of absorbable metals for biomedical applications, Prog. Biomater. 7 (2018) 93–110, doi:10.1007/s40204-018-0091-4.

[4] R. Gorejová, L. Haverová, R. Oriňaková, A. Oriňak, M. Oriňak, Recent advancements in Fe-based biodegradable materials for bone repair, J. Mater. Sci. 54 (2019) 1913–1947, doi:10.1007/s10853-018-3011-z.

[5] J.C. Reichert, M.E. Wullschleger, A. Cipitria, J. Lienau, T.K. Cheng, M.A. Schütz, G.N. Duda, U. Nöth, J. Eulert, D.W. Hutmacher, Custom-made composite scaffolds for segmental defect repair in long bones, Int. Orthop. 35 (2011) 1229–1236, doi:10.1007/s00264-010-1146-x.

[6] S. Bose, S. Vahabzadeh, A. Bandyopadhyay, Bone tissue engineering using 3D printing, Mater. Today. 16 (2013) 496–504, doi:10.1016/j.mattod.2013.11.017.

[7] L. Li, F. Yu, J. Shi, S. Shen, H. Teng, J. Yang, X. Wang, Q. Jiang, In situ repair of bone and cartilage defects using 3D scanning and 3D printing, Sci. Rep. 7 (2017) 1–12, doi:10.1038/s41598-017-10060-3.

[8] X. Wang, S. Xu, S. Zhou, W. Xu, M. Leary, P. Choong, M. Qian, M. Brandt, Y.M. Xie, Topological design and additive manufacturing of porous metals for bone scaffolds and orthopaedic implants: a review, Biomaterials 83 (2016) 127–141, doi:10.1016/j.biomaterials.2016.01.012.

[9] X.Y. Zhang, G. Fang, J. Zhou, Additively manufactured scaffolds for bone tissue engineering and the prediction of their mechanical behavior: a review, Materials 10 (2017) 50, doi:10.3390/ma10010050.

[10] G. Li, L. Wang, W. Pan, F. Yang, W. Jiang, X. Wu, X. Kong, K. Dai, Y. Hao, *In vitro* and *in vivo* study of additive manufactured porous Ti$_6$Al$_4$V scaffolds for repairing bone defects, Sci. Rep. 6 (2016) 1–11, doi:10.1038/srep34072.

[11] V. Karageorgiou, D. Kaplan, Porosity of 3D biomaterial scaffolds and osteogenesis, Biomaterials 26 (2005) 5474–5491, doi:10.1016/j.biomaterials.2005.02.002.

[12] Y. Li, P. Pavanram, J. Zhou, K. Lietaert, P. Taheri, W. Li, H. San, M.A. Leeflang, J.M.C. Mol, H. Jahr, A.A. Zadpoor, Additively manufactured biodegradable porous zinc, Acta Biomater 101 (2020) 609–623, doi:10.1016/j.actbio.2019.10.034.

[13] S. Romanazzo, T.G. Molley, S. Nemec, K. Lin, R. Sheikh, J.J. Gooding, B. Wan, Q. Li, K.A. Kilian, I. Roohani, Synthetic bone-like structures through omnidirectional ceramic bioprinting in cell suspensions, Adv. Funct. Mater. 31 (2021) 1–12, doi:10.1002/adfm.202008216.

[14] L. Tan, X. Yu, P. Wan, K. Yang, Biodegradable materials for bone repairs: a review, J. Mater. Sci. Technol. 29 (2013) 503–513, doi:10.1016/j.jmst.2013.03.002.

[15] Z. Sheikh, S. Najeeb, Z. Khurshid, V. Verma, H. Rashid, M. Glogauer, Biodegradable materials for bone repair and tissue engineering applications, Materials 8 (2015) 5744–5794, doi:10.3390/ma8095273.

[16] G.L. Koons, M. Diba, A.G. Mikos, Materials design for bone-tissue engineering, Nat. Rev. Mater. 5 (2020) 584–603, doi:10.1038/s41578-020-0204-2.

[17] A.H. Yusop, A. Al Sakkaf, H. Nur, Modifications on porous absorbable Fe-based scaffolds for bone applications : a review from corrosion and biocompatibility viewpoints, J. Biomed. Mater. Res. Part B (2021) 1–27, doi:10.1002/jbm.b.34893.

[18] N.A. Zumdick, L. Jauer, L.C. Kersting, T.N. Kutz, J.H. Schleifenbaum, D. Zander, Additive manufactured WE43 magnesium: a comparative study of the microstructure and mechanical properties with those of powder extruded and as-cast WE43, Mater. Charact. 147 (2019) 384–397, doi:10.1016/j.matchar.2018.11.011.

[19] P. Wen, M. Voshage, L. Jauer, Y. Chen, Y. Qin, R. Poprawe, J.H. Schleifenbaum, Laser additive manufacturing of Zn metal parts for biodegradable applications: processing, formation quality and mechanical properties, Mater. Des. 155 (2018) 36–45, doi:10.1016/j.matdes.2018.05.057.

[20] B. Song, S. Dong, S. Deng, H. Liao, C. Coddet, Microstructure and tensile properties of iron parts fabricated by selective laser melting, Opt. Laser Technol. 56 (2014) 451–460, doi:10.1016/j.optlastec.2013.09.017.

[21] L. Zhang, B. Song, S.K. Choi, Y. Shi, A topology strategy to reduce stress shielding of additively manufactured porous metallic biomaterials, Int. J. Mech. Sci. 197 (2021) 106331, doi:10.1016/j.ijmecsci.2021.106331.

[22] Y. Li, H. Jahr, P. Pavanram, F.S.L. Bobbert, U. Puggi, X.Y. Zhang, B. Pouran, M.A. Leeflang, H. Weinans, J. Zhou, A.A. Zadpoor, Additively manufactured functionally graded biodegradable porous iron, Acta Biomater 96 (2019) 646–661, doi:10.1016/j.actbio.2019.07.013.

[23] C. Yang, Z. Huan, X. Wang, C. Wu, J. Chang, 3D Printed Fe scaffolds with HA nanocoating for bone regeneration, ACS Biomater. Sci. Eng. 4 (2018) 608–616, doi:10.1021/acsbiomaterials.7b00885.

[24] A. Sharipova, S.K. Swain, I. Gotman, D. Starosvetsky, S.G. Psakhie, R. Unger, E.Y. Gutmanas, Mechanical, degradation and drug-release behavior of nanograined Fe-Ag composites for biomedical applications, J. Mech. Behav. Biomed. Mater. 86 (2018) 240–249, doi:10.1016/j.jmbbm.2018.06.037.

[25] A. Sharipova, I. Gotman, S.G. Psakhie, E.Y. Gutmanas, Biodegradable nanocomposite Fe–Ag load-bearing scaffolds for bone healing, J. Mech. Behav. Biomed. Mater. 98 (2019) 246–254, doi:10.1016/j.jmbbm.2019.06.033.

[26] Y.P. Feng, N. Gaztelumendi, J. Fornell, H.Y. Zhang, P. Solsona, M.D. Baró, S. Suriñach, E. Ibáñez, L. Barrios, E. Pellicer, C. Nogués, J. Sort, Mechanical

properties, corrosion performance and cell viability studies on newly developed porous Fe-Mn-Si-Pd alloys, J. Alloys Compd. 724 (2017) 1046–1056, doi:10.1016/j.jallcom.2017.07.112.

[27] M.S. Dargusch, A. Dehghan-Manshadi, M. Shahbazi, J. Venezuela, X. Tran, J. Song, N. Liu, C. Xu, Q. Ye, C. Wen, Exploring the role of manganese on the microstructure, mechanical properties, biodegradability, and biocompatibility of porous iron-based scaffolds, ACS Biomater. Sci. Eng. 5 (2019) 1686–1702, doi:10.1021/acsbiomaterials.8b01497.

[28] C. Shuai, W. Yang, Y. Yang, H. Pan, C. He, F. Qi, D. Xie, H. Liang, Selective laser melted Fe-Mn bone scaffold: microstructure, corrosion behavior and cell response, Mater. Res. Express. 7 (2019) 015404, doi:10.1088/2053-1591/ab62f5.

[29] P. Liu, D. Zhang, Y. Dai, J. Lin, Y. Li, C. Wen, Microstructure, mechanical properties, degradation behavior, and biocompatibility of porous Fe-Mn alloys fabricated by sponge impregnation and sintering techniques, Acta Biomater. 114 (2020) 485–496, doi:10.1016/j.actbio.2020.07.048.

[30] N.E. Putra, M.A. Leeflang, P. Taheri, L.E. Fratila-Apachitei, J.M.C. Mol, J. Zhou, A.A. Zadpoor, Extrusion-based 3D printing of ex situ-alloyed highly biodegradable MRI-friendly porous iron-manganese scaffolds, Acta Biomater. 134 (2021) 774–790, doi:10.1016/j.actbio.2021.07.042.

[31] P. Sotoudehbagha, S. Sheibani, M. Khakbiz, S. Ebrahimi-Barough, H. Hermawan, Novel antibacterial biodegradable Fe-Mn-Ag alloys produced by mechanical alloying, Mater. Sci. Eng. C. 88 (2018) 88–94, doi:10.1016/j.msec.2018.03.005.

[32] M. Caligari Conti, B. Mallia, E. Sinagra, P. Schembri Wismayer, J. Buhagiar, D. Vella, The effect of alloying elements on the properties of pressed and non-pressed biodegradable Fe–Mn–Ag powder metallurgy alloys, Heliyon 5 (2019) e02522, doi:10.1016/j.heliyon.2019.e02522.

[33] P. Sotoudeh Bagha, M. Khakbiz, S. Sheibani, H. Hermawan, Design and characterization of nano and bimodal structured biodegradable Fe-Mn-Ag alloy with accelerated corrosion rate, J. Alloys Compd. 767 (2018) 955–965, doi:10.1016/j.jallcom.2018.07.206.

[34] T. Huang, J. Cheng, Y.F. Zheng, *In vitro* degradation and biocompatibility of Fe-Pd and Fe-Pt composites fabricated by spark plasma sintering, Mater. Sci. Eng. C. 35 (2014) 43–53, doi:10.1016/j.msec.2013.10.023.

[35] J. Čapek, Š. Msallamová, E. Jablonská, J. Lipov, D. Vojtěch, A novel high-strength and highly corrosive biodegradable Fe-Pd alloy: structural, mechanical and *in vitro* corrosion and cytotoxicity study, Mater. Sci. Eng. C. 79 (2017) 550–562, doi:10.1016/j.msec.2017.05.100.

[36] Y. Li, H. Jahr, K. Lietaert, P. Pavanram, A. Yilmaz, L.I. Fockaert, M.A. Leeflang, B. Pouran, Y. Gonzalez-Garcia, H. Weinans, J.M.C. Mol, J. Zhou, A.A. Zadpoor, Additively manufactured biodegradable porous iron, Acta Biomater. 77 (2018) 380–393, doi:10.1016/j.actbio.2018.07.011.

[37] N.E. Putra, M.A. Leeflang, M. Minneboo, P. Taheri, L.E. Fratila-Apachitei, J.M.C. Mol, J. Zhou, A.A. Zadpoor, Extrusion-based 3D printed biodegradable porous iron, Acta Biomater. 121 (2021) 741–756, doi:10.1016/j.actbio.2020.11.022.

[38] A. Yamamoto, R. Honma, M. Sumita, Cytotoxicity evaluation of 43 metal salts using murine fibroblasts and osteoblastic cells, J. Biomed. Mater. Res. 39 (1998) 331–340 https://doi.org/10.1002/(SICI)1097-4636(199802)39:2⟨331::AID-JBM22⟩3.0.CO;2-E.

[39] C. Gao, M. Yao, C. Shuai, P. Feng, S. Peng, Advances in biocermets for bone implant applications, Bio-Des. Manuf. 3 (2020) 307–330, doi:10.1007/s42242-020-00087-3.

[40] M.F. Ulum, A. Arafat, D. Noviana, A.H. Yusop, A.K. Nasution, M.R. Abdul Kadir, H. Hermawan, *In vitro* and *in vivo* degradation evaluation of novel iron-bioceramic composites for bone implant applications, Mater. Sci. Eng. C. 36 (2014) 336–344, doi:10.1016/j.msec.2013.12.022.

[41] M.F. Ulum, A.K. Nasution, A.H. Yusop, A. Arafat, M.R.A. Kadir, V. Juniantito, D. Noviana, H. Hermawan, Evidences of *in vivo* bioactivity of Fe-bioceramic composites for temporary bone implants, J. Biomed. Mater. Res. Part B 103 (2015) 1354–1365, doi:10.1002/jbm.b.33315.

[42] M. Dehestani, E. Adolfsson, L.A. Stanciu, Mechanical properties and corrosion behavior of powder metallurgy iron-hydroxyapatite composites for biodegradable implant applications, Mater. Des. 109 (2016) 556–569, doi:10.1016/j.matdes.2016.07.092.

[43] A. Reindl, R. Borowsky, S.B. Hein, J. Geis-Gerstorfer, P. Imgrund, F. Petzoldt, Degradation behavior of novel Fe/ß-TCP composites produced by powder injection molding for cortical bone replacement, J. Mater. Sci. 49 (2014) 8234–8243, doi:10.1007/s10853-014-8532-5.

[44] F. He, G. Qian, W. Ren, J. Ke, P. Fan, X. Shi, Y. Cheng, S. Wu, X. Deng, J. Ye, Preparation and characterization of iron/β-tricalcium phosphate bio-cermets for load-bearing bone substitutes, Ceram. Int. 43 (2017) 8348–8355, doi:10.1016/j.ceramint.2017.03.173.

[45] E.B. Montufar, M. Casas-Luna, M. Horynová, S. Tkachenko, Z. Fohlerová, S. Diaz-de-la-Torre, K. Dvořák, L. Čelko, J. Kaiser, High strength, biodegradable and cytocompatible alpha tricalcium phosphate-iron composites for temporal reduction of bone fractures, Acta Biomater. 70 (2018) 293–303, doi:10.1016/j.actbio.2018.02.002.

[46] S. Wang, Y. Xu, J. Zhou, H. Li, J. Chang, Z. Huan, *In vitro* degradation and surface bioactivity of iron-matrix composites containing silicate-based bioceramic, Bioact. Mater. 2 (2017) 10–18, doi:10.1016/j.bioactmat.2016.12.001.

[47] H. Ma, T. Li, Z. Huan, M. Zhang, Z. Yang, J. Wang, J. Chang, C. Wu, 3D printing of high-strength bioscaffolds for the synergistic treatment of bone cancer, NPG Asia Mater 10 (2018) 31–44, doi:10.1038/s41427-018-0015-8.

[48] M. Sikora-Jasinska, C. Paternoster, E. Mostaed, R. Tolouei, R. Casati, M. Vedani, D. Mantovani, Synthesis, mechanical properties and corrosion behavior of powder metallurgy processed Fe/Mg2Si composites for biodegradable implant applications, Mater. Sci. Eng. C. 81 (2017) 511–521, doi:10.1016/j.msec.2017.07.049.

[49] M. Sikora-Jasinska, P. Chevallier, S. Turgeon, C. Paternoster, E. Mostaed, M. Vedani, D. Mantovani, Long-term *in vitro* degradation behaviour of Fe and Fe/Mg_2Si composites for biodegradable implant applications, RSC Adv. 8 (2018) 9627–9639, doi:10.1039/c8ra00404h.

[50] M. Sikora-Jasinska, P. Chevallier, S. Turgeon, C. Paternoster, E. Mostaed, M. Vedani, D. Mantovani, Understanding the effect of the reinforcement addition on corrosion behavior of Fe/Mg_2Si composites for biodegradable implant applications, Mater. Chem. Phys. 223 (2019) 771–778, doi:10.1016/j.matchemphys.2018.11.068.

[51] C. Shuai, Y. Li, Y. Yang, S. Peng, W. Yang, F. Qi, S. Xiong, H. Liang, L. Shen, Bioceramic enhances the degradation and bioactivity of iron bone implant, Mater. Res. Express. 6 (2019), doi:10.1088/2053-1591/ab45b9.

[52] C. Gao, M. Yao, S. Li, P. Feng, S. Peng, C. Shuai, Highly biodegradable and bioactive Fe-Pd-bredigite biocomposites prepared by selective laser melting, J. Adv. Res. 20 (2019) 91–104, doi:10.1016/j.jare.2019.06.001.

[53] M. Diba, O.M. Goudouri, F. Tapia, A.R. Boccaccini, Magnesium-containing bioactive polycrystalline silicate-based ceramics and glass-ceramics for biomedical applications, Curr. Opin. Solid State Mater. Sci. 18 (2014) 147–167, doi:10.1016/j.cossms.2014.02.004.

[54] K. Bavya Devi, S.K. Nandi, M. Roy, Magnesium silicate bioceramics for bone regeneration: a review, J. Indian Inst. Sci. 99 (2019) 261–288, doi:10.1007/s41745-019-00119-7.

[55] S. Yoshizawa, A. Brown, A. Barchowsky, C. Sfeir, Magnesium ion stimulation of bone marrow stromal cells enhances osteogenic activity, simulating the effect of magnesium alloy degradation, Acta Biomater. 10 (2014) 2834–2842, doi:10.1016/j.actbio.2014.02.002.

[56] M.Q. Cheng, T. Wahafu, G.F. Jiang, W. Liu, Y.Q. Qiao, X.C. Peng, T. Cheng, X.L. Zhang, G. He, X.Y. Liu, A novel open-porous magnesium scaffold with controllable microstructures and properties for bone regeneration, Sci. Rep. 6 (2016) 1–14, doi:10.1038/srep24134.

[57] K. Szurkowska, J. Kolmas, Hydroxyapatites enriched in silicon – Bioceramic materials for biomedical and pharmaceutical applications, Prog. Nat. Sci. Mater. Int. 27 (2017) 401–409, doi:10.1016/j.pnsc.2017.08.009.

[58] A.F. Khan, M. Saleem, A. Afzal, A. Ali, A. Khan, A.R. Khan, Bioactive behavior of silicon substituted calcium phosphate based bioceramics for bone regeneration, Mater. Sci. Eng. C. 35 (2014) 245–252, doi:10.1016/j.msec.2013.11.013.

[59] Y. Huang, X. Jin, X. Zhang, H. Sun, J. Tu, T. Tang, J. Chang, K. Dai, *In vitro* and *in vivo* evaluation of akermanite bioceramics for bone regeneration, Biomaterials 30 (2009) 5041–5048, doi:10.1016/j.biomaterials.2009.05.077.

[60] L. Xia, Z. Yin, L. Mao, X. Wang, J. Liu, X. Jiang, Z. Zhang, K. Lin, J. Chang, B. Fang, Akermanite bioceramics promote osteogenesis, angiogenesis and suppress osteoclastogenesis for osteoporotic bone regeneration, Sci. Rep. 6 (2016) 1–17, doi:10.1038/srep22005.

[61] W. Liu, T. Wang, X. Zhao, X. Dan, W.W. Lu, H. Pan, Akermanite used as an alkaline biodegradable implants for the treatment of osteoporotic bone defect, Bioact. Mater. 1 (2016) 151–159, doi:10.1016/j.bioactmat.2016.11.004.

[62] Y. Huang, C. Wu, X. Zhang, J. Chang, K. Dai, Regulation of immune response by bioactive ions released from silicate bioceramics for bone regeneration, Acta Biomater. 66 (2018) 81–92, doi:10.1016/j.actbio.2017.08.044.

[63] C. Wu, J. Chang, Synthesis and apatite-formation ability of akermanite, Mater. Lett. 58 (2004) 2415–2417, doi:10.1016/j.matlet.2004.02.039.

[64] ASTM B963-17Standard Test Methods For Oil content, Oil-Impregnation efficiency, and Surface-Connected Porosity of Sintered Powder Metallurgy (PM) Products Using Archimedes' Principle, ASTM International, 2017, doi:10.1520/B0963-14.

[65] A. Oyane, H.M. Kim, T. Furuya, T. Kokubo, T. Miyazaki, T. Nakamura, Preparation and assessment of revised simulated body fluids, J. Biomed. Mater. Res. Part A. 65 (2003) 188–195, doi:10.1002/jbm.a.10482.

[66] L. Yang, E. Zhang, Biocorrosion behavior of magnesium alloy in different simulated fluids for biomedical application, Mater. Sci. Eng. C. 29 (2009) 1691–1696, doi:10.1016/j.msec.2009.01.014.

[67] ASTM G1-03, Standard practice for preparing, cleaning, and evaluating corrosion test specimens, ASTM Int. (2017), doi:10.1520/G0001-03R17E01.2.

[68] ASTM G32-72, Standard practice for laboratory immersion corrosion testing of metals, ASTM Int. (2004), doi:10.1520/G0031-72R04.2.

[69] ISO 13314, Mechanical testing of metals - Ductility testing - Compression test for porous and cellular metals, Int. Organ. Stand. (2011) www.iso.org.

[70] C. Valero, A. Igual, Electrochemical aspects in biomedical alloy characterization: electrochemical impedance spectrosopy, Biomed. Eng. Trends Mater. Sci. (2011), doi:10.5772/13039.

[71] J. Tedim, M.L. Zheludkevich, A.C. Bastos, A.N. Salak, A.D. Lisenkov, M.G.S. Ferreira, Influence of preparation conditions of layered double hydroxide conversion films on corrosion protection, Electrochim. Acta. 117 (2014) 164–171, doi:10.1016/j.electacta.2013.11.111.

[72] B. Van der Linden, H. Terryn, J. Vereecken, Investigation of anodic aluminium oxide layers by electrochemical impedance spectroscopy, J. Appl. Electrochem. 20 (1990) 798–803, doi:10.1007/BF01094309.

[73] ISO 10993-5Tests for *In Vitro* Cytotoxicity, International Organization for Standardization, 2009, doi:10.1021/es0620181.

[74] E.F. Morgan, G.U. Unnikrisnan, A.I. Hussein, Bone mechanical properties in healthy and diseased states, Annu. Rev. Biomed. Eng. 20 (2018) 119–143, doi:10.1146/annurev-bioeng-062117-121139.

[75] A. Ribeiro, M.M. Blokzijl, R. Levato, C.W. Visser, M. Castilho, W.E. Hennink, T. Vermonden, J. Malda, Assessing bioink shape fidelity to aid material development in 3D bioprinting, Biofabrication 10 (2018), doi:10.1088/1758-5090/aa90e2.

[76] C. Duty, C. Ajinjeru, V. Kishore, B. Compton, N. Hmeidat, X. Chen, P. Liu, A.A. Hassen, J. Lindahl, V. Kunc, What makes a material printable? A viscoelastic model for extrusion-based 3D printing of polymers, J. Manuf. Process. 35 (2018) 526–537, doi:10.1016/j.jmapro.2018.08.008.

[77] A.F. Bonatti, I. Chiesa, G. Vozzi, C. De Maria, Open-source CAD-CAM simulator of the extrusion-based bioprinting process, Bioprinting 24 (2021) e00172, doi:10.1016/j.bprint.2021.e00172.

[78] N. Paxton, W. Smolan, T. Böck, F. Melchels, J. Groll, T. Jungst, Proposal to assess printability of bioinks for extrusion-based bioprinting and evaluation of rheological properties governing bioprintability, Biofabrication (2017) 9, doi:10.1088/1758-5090/aa8dd8.

[79] R. Marunaka, M. Kawaguchi, Rheological behavior of hydrophobic fumed silica suspensions in aromatic dispersion media, J. Dispers. Sci. Technol. 38 (2017) 223–228, doi:10.1080/01932691.2016.1155154.

[80] J. He, H. Ye, Y. Li, J. Fang, Q. Mei, X. Lu, F. Ren, Cancellous-bone-like porous iron scaffold coated with strontium incorporated octacalcium phosphate nanowhiskers for bone regeneration, ACS Biomater. Sci. Eng. 5 (2019) 509–518, doi:10.1021/acsbiomaterials.8b01188.

[81] M.C. Ratri, A.I. Brilian, A. Setiawati, H.T. Nguyen, V. Soum, K. Shin, Recent advances in regenerative tissue fabrication: tools, materials, and microenvironment in hierarchical aspects, Adv. NanoBiomed Res. 1 (2021) 2000088, doi:10.1002/anbr.202000088.

[82] S. Debnath, R. Ranade, S.L. Wunder, J. McCool, K. Boberick, G. Baran, Interface effects on mechanical properties of particle-reinforced composites, Dent. Mater. 20 (2004) 677–686, doi:10.1016/j.dental.2003.12.001.

[83] S.Y. Fu, X.Q. Feng, B. Lauke, Y.W. Mai, Effects of particle size, particle/matrix interface adhesion and particle loading on mechanical properties of particulate-polymer composites, Compos. Part B 39 (2008) 933–961, doi:10.1016/j.compositesb.2008.01.002.

[84] Y. Su, Q. Ouyang, W. Zhang, Z. Li, Q. Guo, G. Fan, D. Zhang, Composite structure modeling and mechanical behavior of particle reinforced metal matrix composites, Mater. Sci. Eng. A. 597 (2014) 359–369, doi:10.1016/j.msea.2014.01.024.

[85] C. Wu, J. Chang, S. Ni, J. Wang, *In vitro* bioactivity of akermanite ceramics, J. Biomed. Mater. Res. Part A. 76 (2006) 73–80, doi:10.1002/jbm.a.30496.

[86] E. Mouzou, C. Paternoster, R. Tolouei, P. Chevallier, C.A. Biffi, A. Tuissi, D. Mantovani, CO2-rich atmosphere strongly affects the degradation of Fe-21Mn-1C for biodegradable metallic implants, Mater. Lett. 181 (2016) 362–366, doi:10.1016/j.matlet.2016.06.017.

[87] S.Y. Yang, H.H. Chang, C.J. Lin, S.J. Huang, J.C.C. Chan, Is Mg-stabilized amorphous calcium carbonate a homogeneous mixture of amorphous magnesium carbonate and amorphous calcium carbonate? Chem. Commun. 52 (2016) 11527–11530, doi:10.1039/c6cc04522g.

[88] J. Zhang, C. Dong, Y. Sun, J. Yu, Mechanism of magnesium's influence on calcium carbonate crystallization: kinetically controlled multistep crystallization, Cryst. Res. Technol. 53 (2018) 1–8, doi:10.1002/crat.201800075.

[89] M. Kellermeier, E. Melero-García, F. Glaab, R. Klein, M. Drechsler, R. Rachel, J.M. García-Ruiz, W. Kunz, Stabilization of amorphous calcium carbonate in inorganic silica-rich environments, J. Am. Chem. Soc. 132 (2010) 17859–17866, doi:10.1021/ja106959p.

[90] F. Witte, V. Kaese, H. Haferkamp, E. Switzer, A. Meyer-Lindenberg, C.J. Wirth, H. Windhagen, *In vivo* corrosion of four magnesium alloys and the associated bone response, Biomaterials 26 (2005) 3557–3563, doi:10.1016/j.biomaterials.2004.09.049.

[91] C.J.S. Ibsen, D. Chernyshov, H. Birkedal, Apatite formation from amorphous calcium phosphate and mixed amorphous calcium phosphate/amorphous calcium carbonate, Chem. A Eur. J. 22 (2016) 12347–12357, doi:10.1002/chem.201601280.

[92] K. Ishikawa, K. Hayashi, Carbonate apatite artificial bone, Sci. Technol. Adv. Mater. 22 (2021) 683–694, doi:10.1080/14686996.2021.1947120.

[93] P. Opitz, L. Besch, M. Panthöfer, A. Kabelitz, R.E. Unger, F. Emmerling, M. Mondeshki, W. Tremel, Insights into the *in vitro* formation of apatite from Mg-stabilized amorphous calcium carbonate, Adv. Funct. Mater. 31 (2021) 2007830, doi:10.1002/adfm.202007830.

[94] M. Mozafari, S. Banijamali, F. Baino, S. Kargozar, R.G. Hill, Calcium carbonate: adored and ignored in bioactivity assessment, Acta Biomater. 91 (2019) 35–47, doi:10.1016/j.actbio.2019.04.039.

[95] A. Xu, F. Zhang, F. Jin, R. Zhang, B. Luo, T. Zhang, The evaluation of coating performance by analyzing the intersection of Bode plots, Int. J. Electrochem. Sci. 9 (2014) 5125.

[96] C. Wu, J. Chang, Degradation, bioactivity, and cytocompatibility of diopside, akermanite, and bredigite ceramics, J. Biomed. Mater. Res. 83 (2007) 153–160, doi:10.1002/jbmb.

[97] S. Ni, J. Chang, *In vitro* degradation, bioactivity, and cytocompatibility of calcium silicate, dimagnesium silicate, and tricalcium phosphate bioceramics, J. Biomater. Appl. 24 (2009) 139–158, doi:10.1177/0885328208094745.

[98] R. Oriňaková, R. Gorejová, Z.O. Králová, A. Oriňak, I. Shepa, J. Hovancová, A. Kovalčíková, Z.L. Bujňáková, N. Király, M. Kaňuchová, M. Baláž, M. Strečková, M. Kupková, M. Hrubovčáková, F. Kaľavský, M. Oriňak, Influence of albumin interaction on corrosion resistance of sintered iron biomaterials with polyethyleneimine coating, Appl. Surf. Sci. 509 (2020) 145379, doi:10.1016/j.apsusc.2020.145379.

[99] P. Feng, C. Gao, C. Shuai, S. Peng, Toughening and strengthening mechanisms of porous akermanite scaffolds reinforced with nano-titania, RSC Adv. 5 (2015) 3498–3507, doi:10.1039/c4ra12095g.

[100] Y. Lin, H. Chen, C.M. Chan, J. Wu, High impact toughness polypropylene/$CaCO_3$ nanocomposites and the toughening mechanism, Macromolecules 41 (2008) 9204–9213, doi:10.1021/ma801095d.

[101] S. Menbari, F. Ashenai Ghasemi, I. Ghasemi, Simultaneous improvement in the strength and toughness of polypropylene by incorporating hybrid graphene/$CaCO_3$ reinforcement, Polym. Test. 54 (2016) 281–287, doi:10.1016/j.polymertesting.2016.07.026.

[102] Y.F. He, Y. Ma, C. Gao, G.Y. Zhao, L.L. Zhang, G.F. Li, Y.Z. Pan, K. Li, Y.J. Xu, Iron overload inhibits osteoblast biological activity through oxidative stress, Biol. Trace Elem. Res. 152 (2013) 292–296, doi:10.1007/s12011-013-9605-z.

[103] Y.B. Wang, X.H. Xie, H.F. Li, X.L. Wang, M.Z. Zhao, E.W. Zhang, Y.J. Bai, Y.F. Zheng, L. Qin, Biodegradable CaMgZn bulk metallic glass for potential skeletal application, Acta Biomater. 7 (2011) 3196–3208, doi:10.1016/j.actbio.2011.04.027.

[104] T. Kihara, M. Hirose, A. Oshima, H. Ohgushi, Exogenous type I collagen facilitates osteogenic differentiation and acts as a substrate for mineralization of rat marrow mesenchymal stem cells *in vitro*, Biochem. Biophys. Res. Commun. 341 (2006) 1029–1035, doi:10.1016/j.bbrc.2006.01.059.

[105] Z. Xu, K.G. Neoh, A. Kishen, A biomimetic strategy to form calcium phosphate crystals on type i collagen substrate, Mater. Sci. Eng. C. 30 (2010) 822–826, doi:10.1016/j.msec.2010.03.014.

[106] Q. Liu, L. Cen, S. Yin, L. Chen, G. Liu, J. Chang, L. Cui, A comparative study of proliferation and osteogenic differentiation of adipose-derived stem cells on akermanite and β-TCP ceramics, Biomaterials 29 (2008) 4792–4799, doi:10.1016/j.biomaterials.2008.08.039.

[107] H. Sun, C. Wu, K. Dai, J. Chang, T. Tang, Proliferation and osteoblastic differentiation of human bone marrow-derived stromal cells on akermanite-bioactive ceramics, Biomaterials 27 (2006) 5651–5657, doi:10.1016/j.biomaterials.2006.07.027.